Computational simulation of aircraft electrothermal de-icing using an unsteady formulation of phase change and runback water in a unified framework

Esmaeil Esmaeilifar[a], L. Prince Raj[b], R.S. Myong[a,*]

[a]School of Mechanical and Aerospace Engineering, and ACTRC, Gyeongsang National University, 501 Jinjudaero, Jinju, Gyeongnam 52828, South Korea

[b]Department of Aerospace Engineering and Applied Mechanics, Indian Institute of Engineering Science and Technology, Shibpur, Howrah,711103, India

*Corresponding author. E-mail address: *myong@gnu.ac.kr* (R.S. Myong)

Abstract

Accurately predicting de-icing processes is essential to ensure the proper sizing and design of ice protection systems in aircraft icing. A unified framework was developed to simulate an unsteady electrothermal de-icing process, using an unsteady formulation to account for phase change and runback water. Two physically-motivated concepts were newly introduced to the icing model to accurately describe the unsteady electrothermal de-icing (ice accretion/melting) process. A conjugate heat transfer method was utilized to tightly couple the ice and conduction solvers. Sub-iterations were incorporated at every time step to ensure the convergence of temperature and heat flux at the interface. The unsteady de-icing framework consists of a compressible Navier-Stokes-Fourier airflow solver, Eulerian droplet impingement solver, unsteady ice accretion/melting solver, and heat conduction solver, which can handle multilayer composite materials. All solvers were formulated based on partial differential equations and developed in a unified finite volume framework, enabling the use of a single grid system and eliminating unnecessary grid generation for the ice layer. The results showed better agreement with experimental data compared to other results. The unified solver was used to analyze the unsteady electrothermal de-icing process by investigating the ice accretion, ice melting, runback water film, and freezing of water film in unprotected areas. Runback water film due to ice melting may exceed the impingement limits and freeze in unprotected areas, leading to ice ridge formation.

Keywords: Aircraft icing; electrothermal de-icing; phase change; unsteady formulation; CFD

1. Introduction

Aircraft icing occurs when an aircraft flies through icing clouds and supercooled water droplets impinge on the aircraft's surface [1-4]. Ice accretion on critical components of an aircraft like the wing leading edge, engine inlet, pitot tube, and cockpit windows can cause severe safety problems [5]. For instance, ice accumulation on the wing can reduce aerodynamic performance by changing the aerodynamic shape of the wing [6-9]. Moreover, ice accretion increases drag by altering surface roughness and flow patterns. Asymmetric roughness and ice accretion on the wing or other control surfaces can also degrade stability and handling quality [10, 11]. Accumulated ice on the aircraft or rotorcraft structure can be broken up by aerodynamic forces and vibrations. The ice fragments shed from the surface are detrimental if they hit critical surfaces or are ingested into the engine [12]. Ice particles ingested into the engine can affect thrust production, damage engine components, and even block the engine inlet [13, 14]. For these reasons, ice protection systems (IPS) have been developed to deal with ice accretion on the wing and other critical parts of aircraft.

There are two main approaches to protecting flying vehicles from in-flight icing: anti-icing and de-icing methods. The anti-icing systems prevent ice from accreting on surfaces, which usually requires high energy consumption, especially when operating in fully evaporative mode. On the other hand, the de-icing systems remove the accumulated ice before the ice results in significant aerodynamic penalties. Since de-icing systems allow some ice accretion on the surface, the latent heat of fusion is released which increases the surface temperature. As a result, compared to anti-icing systems, less power is required to melt the ice and clean the surface using de-icing systems [15, 16].

Of all IPS developed to date, the most commonly used are bleed air, electrothermal heater, electro-mechanical impulse system, and pneumatic boot inflation [17]. Pneumatic boot inflation and structural impulse systems require a minimum amount of ice accumulation on the protected surface to function efficiently. The bleed air system uses hot air from the engine to keep the aircraft surface clean aerodynamically, but it penalizes engine performance, especially for small aircraft [18]. The danger of

structural damage due to hot air leakage requires a reliable precooler or leak detection system, which adds weight and complexity to the system.

The electrothermal IPS is based on the Joule heating principle and uses heat to protect the critical parts of aircraft or rotorcraft from in-flight icing. Previously, electrothermal IPS was mainly used for helicopter blades, propellers, and pitot tubes. However, after the introduction of the electrothermal wing IPS in the Boeing 787, it has been proven as the main ice protection system of the aircraft. Some applications of electrothermal IPS for anti-icing and de-icing approaches are illustrated in Fig. 1. Electrothermal IPS utilizes independent heating pads with automatic and adjustable input power, which can be turned on and off sequentially to customize heat distribution on the surface, saving a significant amount of energy compared to the bleed air IPS. Carbon fiber-reinforced polymer (CFRP) composites are widely used in aircraft structures and have a lower thermal conductivity than traditional aluminum structures, making them vulnerable to overheating. Consequently, anti-icing and de-icing systems need to be carefully designed for composite structures [19-22].

(a)

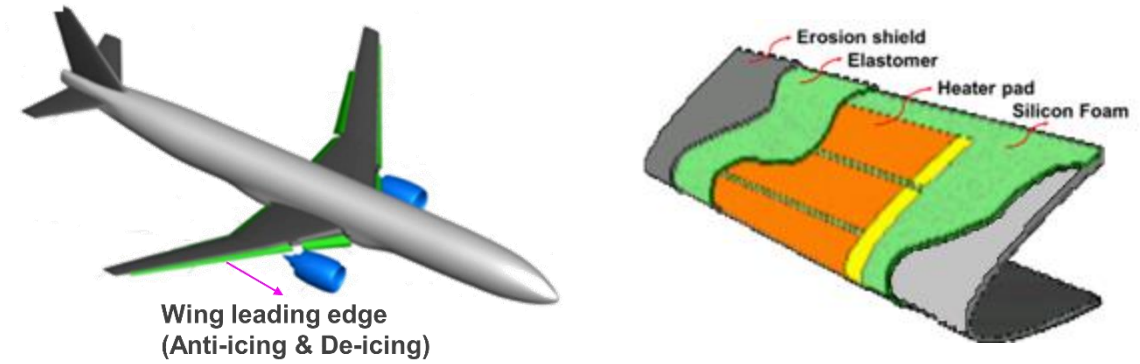

(b)

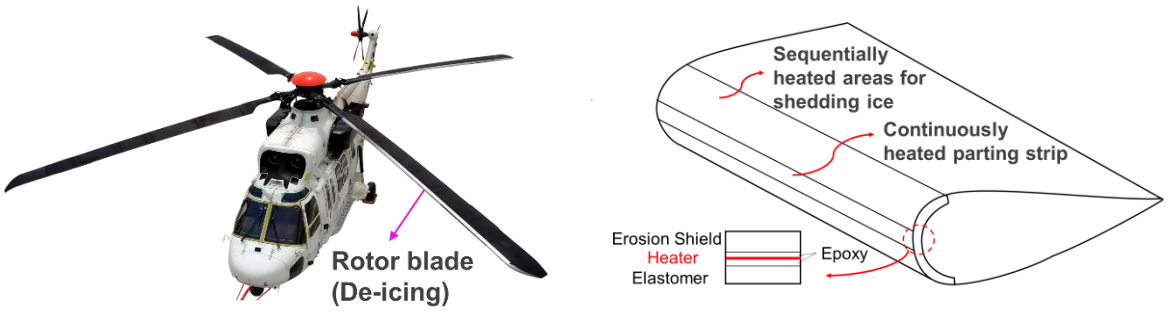

(c)

Fig. 1. Examples of IPS applications: (a) Engine intake of the KAI KUH-1 Surion helicopter (left) and icing test results of a helicopter engine air intake (right); (b) IPS on an airplane wing (left) and schematic of an electro-thermal IPS with heater pads (right); (c) rotor blade of the KAI KUH-1 Surion helicopter (left) and schematic of a rotor blade de-icing system (right).

Numerical modeling of electrothermal de-icing requires a multiphysics framework consisting of different solvers to model airflow, water droplet impingement, phase change, water film dynamics, heat conduction in the substrate, and thermal interactions between solid and fluid domains (Fig. 2). Using the conjugate heat transfer (CHT) method, solid and fluid domains can be coupled by exchanging thermal boundary conditions at the interface [23]. Although the main focus of this study is on modeling the unsteady phase change in the ice layer and runback water, the importance of the role of airflow and droplet impingement cannot be neglected when predicting ice accretion. The convective heat transfer coefficient calculated from the compressible Navier-Stokes-Fourier (NSF) air solver plays a vital role in the heat balance of the ice solver. Also, the wall shear stress is directly used to calculate the mean water film velocity on the surface, which is crucial to accurately predict the runback water film. Further, the droplet solver provides collection efficiency, which represents the potential for ice accretion on the surface.

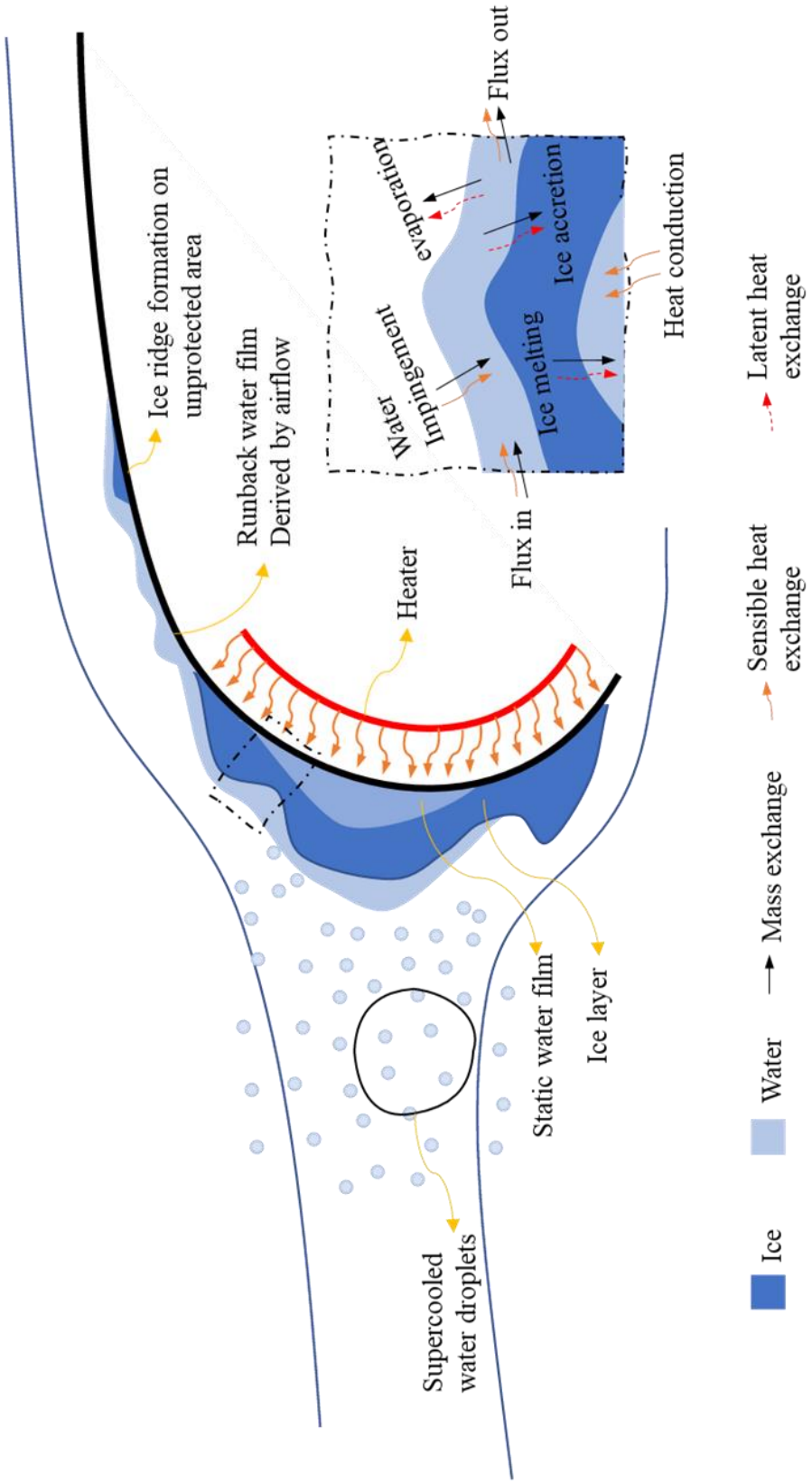

Fig. 2. Schematic illustration of the electrothermal de-icing process in aircraft in-flight icing applications.

During the last four decades, different icing simulation tools such as LEWICE [24], FENSAP-ICE [25], ONERA [26], ICECREMO [27], CANICE [28], and PolimICE [29] have been developed. However, not all of these solvers support electrothermal de-icing simulation. The solvers have differences in modeling airflow, droplet impingement, phase change, and runback water, as summarized in Table 1. Early studies on electrothermal de-icing focused on the heat conduction in a multilayer solid with an existing ice layer on top of it, known as the deicer pad problem [30-32]. The enthalpy method was often used to address the phase change problem in these studies. The heat conduction equation is solved to calculate the temperature distribution in the multilayer solid [33]. The same equation for the enthalpy was utilized to evaluate phase change and to calculate the temperature distribution in the ice layer.

Table 1
Comparison of different de-icing solvers available in the literature.

	Airflow	**Droplet**	**HTC**	**Icing model**	**Phase change**	**Validation**
LEWICE [24]	Potential flow	Lagrangian	IBL	Messinger	Enthalpy method	NASA Lewis IRT experiments
FENSAP [25]	NSF	Eulerian	RANS	PDE (SWIM)	Enthalpy method	NASA Lewis IRT experiments
ONERA [26]	Euler	Eulerian Lagrangian	IBL	PDE	Stefan condition	-
ICECREMO2 [27]	-	Lagrangian	-	Myers	Stefan condition	Deicer pad
Shen et. al [40]	NSF	Eulerian	RANS	Messinger	Unsteady freezing fraction	NASA Lewis IRT experiments
Present (unified)	NSF	Eulerian	RANS	PDE (SWIM)	Unsteady freezing fraction	NASA Lewis IRT experiments

These models only handle melting an existing ice layer on top of the surface and fail to address ice accretion that occurs due to supercooled water impingement during the unsteady de-icing problem. It is worth mentioning that in these methods, ice accretion and de-icing were considered separate problems.

Wright [34] combined these solvers to consider ice accretion in the de-icing problem, which was implemented in the LEWICE code. However, LEWICE uses the panel method to calculate airflow

coupled with the integral boundary layer (IBL) method and heat transfer coefficient on the surface, creating limitations when it comes to accurately predicting airflow around complicated configurations. Further, the LEWICE solver used the Lagrangian ODE-based droplet solver to calculate droplet impingement, and the Messinger model to predict ice accretion. The Lagrangian approach is intuitive, fast, and accurate for 2D and simple geometries. However, the method suffers from severe difficulties with components lying in the shadow of others, and with multiple stagnation points. Furthermore, for 3D and complex geometries such as a rotorcraft rotor blade and engine air intake, the method loses its robustness. For example, it is difficult to determine the tangential trajectories that are directly related to the impingement limit accuracy.

In the second generation of icing simulation tools, Bourgault et al. [35,36] introduced the so-called shallow-water icing model (SWIM)—a PDE-based thermodynamic model to calculate ice accretion and the runback water film. In SWIM, assuming that the water film is very thin and wall shear stress is the only driving force for the water film, the lubrication theory is used to calculate the mean water film velocity. The model enhances the water film prediction by considering the water accumulation in the control volume, which is missing in the Messinger model. In FENSAP, the ice accretion solver was discretized using the explicit finite volume method (FVM), while the airflow, droplet impingement, and heat conduction solvers were discretized using the implicit finite element method (FEM). Reid et al. [25] utilized the SWIM model of FENSAP and the enthalpy method to model the electrothermal de-icing process using the unsteady CHT method. Ice accretion was calculated in the ice solver, while heat conduction in the multilayer solid and melting in the ice layer were calculated in the heat conduction module. Since the ice layer and water film were handled in separate solvers, an extra grid was required for the ice layer in every CHT iteration, and melted water could not contribute to the runback water flow.

Besides the enthalpy method, the Stefan condition and unsteady freezing fraction can be used to predict ice accretion and melting in the ice layer. Considering heat conduction through the ice layer and water film, Myers [37] developed an extended Messinger model. A linear temperature profile was

assumed in each layer, which resulted in a quasi-steady temperature evolution. Phase change was handled using energy balance at the ice/water interface, leading to Stefan's condition. This model was further improved by coupling the water film flow with the icing framework [38]. Harireche et al. [27] extended the runback water and ice accretion model of Myers for anti-icing and de-icing simulations, which were implemented in ICECREMO2. As a part of the ONERA icing framework, Chauvin et al. [39] developed a novel triple-layer icing model with two water layers and one ice layer. Using the triple-layer model and non-overlapping optimized Schwarz method, Bennani et al. [26] conducted an electrothermal de-icing simulation. Shen et al. [40] utilized the unsteady freezing fraction to conduct an electrothermal de-icing simulation. However, they did not consider water accumulation in their model.

In summary, accurate modeling of the unsteady phase change and runback water is essential to accurately predict the de-icing process. The enthalpy method accurately predicts melting in the ice layer, but it requires that grids be generated for the thin ice layer at every coupling step between the ice and conduction solver. Using Stefan's condition to calculate the ice accretion/melting rate may be beneficial because it does not require generating grids for the ice layer. However, it is applicable only for thin ice layers and requires enormous effort to modify ice accretion solvers. The unsteady freezing fraction approach can be implemented easily in the ice accretion solvers, does not require grid generation for the ice layer, and has acceptable accuracy in de-icing applications. The SWIM model is widely used in ice accretion applications due to its robust and accurate runback water prediction. However, the original SWIM model can only estimate wall temperature in the equilibrium state. Consequently, it cannot predict time-accurate temperature during unsteady de-icing simulations.

To solve these shortcomings and unify all solvers into a single system, *this study presents the first computational CHT simulation of the electrothermal de-icing (ice accretion/melting) process for atmospheric icing using an unsteady formulation of phase change and runback water in a unified FVM framework*. The unsteady formulation for phase change was developed based on the unsteady freezing fraction, which is compatible with the unsteady de-icing process. In the new method, the temperature is considered a known quantity in the ice solver, while the wall temperature distribution is calculated in

the heat conduction solver. The unsteady icing model solves both phase change and runback water in the same framework, eliminating the need to generate extra grids for the ice layer. Furthermore, all solvers are coupled using a unified finite volume method framework, which means that a single grid system is used in all solvers. This reduces the additional time needed to generate different grids for different solvers and avoids data loss in the interpolation process from one grid to another.

2. Mathematical and computational models for unsteady ice accretion/melting and de-icing

A brief description of the mathematical and computational models of all four solvers—airflow, droplet impingement, ice accretion/melting, and heat conduction—used for simulating the unsteady de-icing problem are presented in this section. All solvers were developed in a unified FVM framework. A single grid system was used throughout the simulations, facilitating the transfer of information between different solvers.

2.1. Airflow solver

To model the airflow, a finite volume method is used to solve the compressible Navier-Stokes-Fourier (NSF) equations as follows:

$$\begin{bmatrix} \rho_a \\ \rho_a \boldsymbol{u}_a \\ E \end{bmatrix}_t + \nabla \cdot \begin{bmatrix} \rho_a \boldsymbol{u}_a \\ \rho_a \boldsymbol{u}_a \boldsymbol{u}_a + pI \\ (E+p)\boldsymbol{u}_a \end{bmatrix} = \nabla \cdot \begin{bmatrix} 0 \\ \boldsymbol{\tau} \\ \boldsymbol{\tau} \cdot \boldsymbol{u}_a + \boldsymbol{Q} \end{bmatrix}, \tag{1}$$

$$\boldsymbol{\tau} = 2\mu \left[\nabla \boldsymbol{u}_a \right]^{(2)}, \ \boldsymbol{Q} = k \nabla T, \tag{2}$$

where μ and k are the air viscosity and thermal conductivity, respectively. $\boldsymbol{[A]}^{(2)}$ stands for the traceless symmetric part of $\boldsymbol{A}$. An ideal equation of state $p = \rho_a RT$ is used to close the conservation laws (1). The FVM-based air solver couples the NSF equations with the one-equation Spallart-Allmaras (S-A) turbulence model, which also accounts for the rough wall treatment. This turbulence model is computationally efficient and works well for external flows, making it the most used turbulence model in the aircraft icing community.

2.2. Droplet impingement solver

When an aircraft flies through icing clouds, an air-mixed droplet flow field is established around the aircraft. The mass ratio of water droplets to air in a unit volume is on the order of 10^{-3}. Furthermore, the corresponding Stokes number, which characterizes the behavior of the suspended particles in the airflow, is smaller than 0.1 in most icing conditions. In these situations, the effects of droplets on the airflow can be neglected, which makes it possible to solve the air-mixed droplet flow field using a one-way coupling method.

The original Eulerian droplet equations have a non-strictly hyperbolic nature. This problem was circumvented in previous work [41] by splitting the original system into a well-posed part and a source term. Further, the Harten–Lax–van Leer-Contact (HLLC) scheme was developed to ensure the positivity of droplet density in shadow regions, and low droplet density areas near the solid surface. The current Eulerian-based droplet solver is based on the following shallow water type droplet equations (SWDEs),

$$\begin{bmatrix} \rho \\ \rho \boldsymbol{u} \end{bmatrix}_t + \nabla \cdot \begin{bmatrix} \rho \boldsymbol{u} \\ \rho \boldsymbol{u}\boldsymbol{u} + \rho g d \boldsymbol{I} \end{bmatrix} = \begin{bmatrix} 0 \\ A_{\mathbf{u}} \left(\boldsymbol{u}_a - \boldsymbol{u} \right) + \boldsymbol{S}_b + \nabla \cdot \left(\rho g d \boldsymbol{I} \right) \end{bmatrix}. \tag{3}$$

In this equation, d and ρ are the diameter and the density of droplets in terms of liquid water content (LWC). The velocity components of the droplet and air are denoted by $\boldsymbol{u}$, and $\boldsymbol{u}_a$, respectively. $\boldsymbol{S}_b=\rho g[0, 0, 1-\rho_a/\rho_w]^T$, where ρ_w is the density of water and g is the acceleration due to gravity, the result of the force of gravity and the buoyancy of the droplets. A term on the right-hand side, $\nabla \cdot \left(\rho g d \boldsymbol{I} \right)$, is an added source term to circumvent the non-strictly hyperbolic nature of the Eulerian droplet equations [41]. The $A_{\mathbf{u}}(\boldsymbol{u}_a - \boldsymbol{u})$ stands for the aerodynamic drag on droplets caused by airflow, and the coefficient $A_{\mathbf{u}}$ can be expressed as

$$A_{\boldsymbol{u}} = 0.75 \cdot \rho \cdot C_{D_{\boldsymbol{u}}} \cdot \mathrm{Re}_{\boldsymbol{u}} \cdot \mu / \rho_w \cdot \mathrm{MVD}^2, \ \mathrm{Re}_{\mathbf{u}} = \rho_a \cdot \mathrm{MVD} \cdot \left| \boldsymbol{u}_a - \boldsymbol{u} \right| / \mu.$$

2.3. Ice accretion/melting solver

The domain of interest in the ice accretion/melting solver is the ice layer and water film on the surface. The water film thickness in aircraft icing applications is on the order of 10 μm [36]. It is possible to utilize the lubrication theory to predict water film dynamics. Water film height in the normal direction to the wall is very small compared to the chordwise direction. As a result, it is possible to assume that change in the normal direction is negligible and all the physical and thermodynamic variables are constant within a control volume. Since we assumed no change in the normal direction, the grid for the ice and runback water layer was reduced by a dimension. For example, in a 2D icing simulation, the ice grid is one-dimensional, and the grid details of the wall boundary from the air solver are used to make a virtual grid for the ice solver. Considering wall shear stress as the main driving force of the thin water film, water film velocity can be obtained without solving the momentum equation. By integrating over the water film thickness, the shallow-water icing model (SWIM) is obtained as follows:

$$\bar{\boldsymbol{u}}_f = f\left(h_f\right) = \frac{1}{h_f}\int_0^{h_f} u_f dy = \frac{h_f}{2\mu_w}\tau_{wall}, \tag{4}$$

$$\text{where } \boldsymbol{u}_f = \frac{y}{\mu_w}\boldsymbol{\tau}_{wall}. \tag{5}$$

The present ice solver is a PDE-based icing model that solves the mass and energy conservation equations first developed in a previous study [42]. It is further developed in this study to solve the unsteady de-icing problem. In a typical ice accretion problem, the ice solver calculates the ice accretion rate ($\dot{m}_{ice}$), water film thickness (h_f), and equilibrium temperature (T_{equi}) at the surface. However, the original ice solver cannot calculate time-accurate temperature distribution at the wall in an unsteady problem. The reason is that the ice solver can only estimate wall temperature in the equilibrium state. Consequently, it cannot predict unsteady temperature during an unsteady de-icing simulation.

In the new approach, the wall temperature distribution is calculated in the heat conduction solver. In the ice solver, the temperature is considered a known quantity and instead, the de-icing heat load

($\dot{Q}_{de-ice}$) is considered an unknown variable. However, the governing equations remain unchanged, and only some modifications are incorporated into the ice solver:

$$\begin{bmatrix} h_f \\ h_f T_{equi} \end{bmatrix}_t + \nabla \cdot \begin{bmatrix} \frac{h_f^2}{2\mu_w}\boldsymbol{\tau}_{wall} \\ \frac{h_f^2 T_{equi}}{2\mu_w}\boldsymbol{\tau}_{wall} \end{bmatrix} = \begin{bmatrix} \frac{S_M}{\rho_w} \\ \frac{S_E}{\rho_w c_{p,w}} + \frac{T_C S_M}{\rho_w} \end{bmatrix}, \tag{6}$$

$$\begin{aligned} S_M &= \dot{m}_{imp} - \dot{m}_{evap} - \dot{m}_{ice}, \\ S_E &= \left[Cp_w \tilde{T}_{d,\infty} + \frac{\|\boldsymbol{u}_d\|^2}{2} \right] \times \dot{m}_{imp} - L_{evap}\dot{m}_{evap} + h_c\left(T_{equi} - T_\infty\right) + \dot{m}_{ice}\left[L_{fus} - Cp_{ice}T_{equi}\right] + \dot{Q}_{de-ice}, \\ \dot{m}_{imp} &= U_\infty LWC_\infty \beta, \end{aligned} \tag{7}$$

where $\rho_w, \mu_w, Cp_w, Cp_{ice}$ are the density, dynamic viscosity, the specific heat of the water, and the specific heat of ice at constant pressure, respectively. Here $\dot{m}_{imp}$ and $\dot{m}_{evap}$ stand for the instantaneous water droplet impingement mass and instantaneous evaporation mass, respectively. The latent heat of fusion and evaporation are represented by L_{fus} and L_{evap}. Air free-stream velocity, temperature, LWC, and the temperature of the water droplet are denoted by U_∞, T_∞, LWC_∞, $\tilde{T}_{d,\infty}$ respectively. Wall shear stress (τ_{wall}) and convective heat transfer coefficient (h_c) are obtained from the air solver. On the other hand, droplet impact velocity vector ($\boldsymbol{u}_d$) and collection efficiency (β) are transferred from the droplet solver.

2.4. Heat conduction solver

To calculate the temperature inside the solid and the temperature distribution on the solid surface, a heat conduction solver based on the FVM was developed, which can handle multilayer composite materials with different solid properties in each layer,

$$\rho_s Cp_s \frac{\partial T}{\partial t} = \nabla \cdot (k_s \nabla T) + S(t). \quad (8)$$

Here ρ_s, Cp_s are the density and specific heat of the solid, respectively, which can vary for different composite layers. Time-dependent heater fluxes are implemented as a source term, $S(t)$. The new solver is capable of modeling the heater pads implemented between composite layers. It can also handle both structured and unstructured grids. Different boundary conditions, such as Dirichlet, Neumann, and Robin, are implemented to simulate any scenario resulting from the coupling of the heat conduction solver with an ice solver or an airflow solver.

3. The unsteady procedure for electrothermal de-icing

3.1. Overall procedure and flowchart

The unsteady de-icing simulation starts with a clean airflow simulation. Airflow field data consisting of density, velocity, and pressure fields are transferred to the droplet solver. In addition, wall shear stress and the convective heat transfer coefficient from the airflow solver as well as the droplet collection efficiency from the droplet impingement solver are passed to the ice solver. Heat conduction through the solid is calculated in the heat conduction solver, which is tightly coupled with the ice solver. The overall procedure for a de-icing simulation is shown in Fig. 3.

It is worth mentioning that the airflow and droplet impingement results remain unchanged during the unsteady simulation. The reason is that when the ice protection system is turned on (either anti-icing or de-icing), the height of the ice shape is small enough to neglect the effect of ice shape on the airflow field. However, even with very little ice accretion on the surface, the roughness characteristics of the surface can be significantly changed [43, 44]. Consequently, wall roughness should be taken into account in the clean airflow simulation. In this study, a correlation model developed by NASA [45] is used to calculate the equivalent sand-grain roughness corresponding to atmospheric icing conditions.

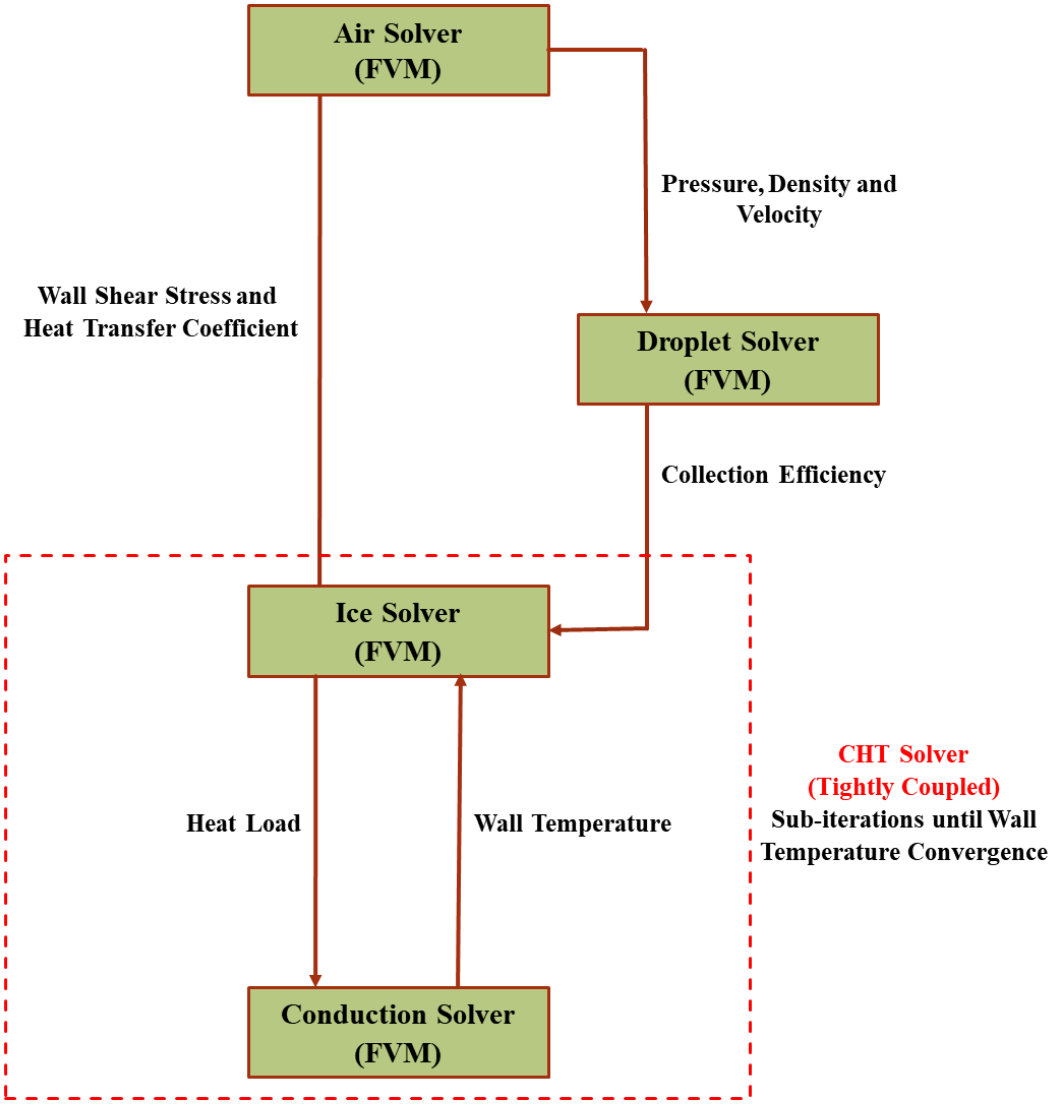

Fig. 3. Unsteady de-icing simulation flowchart.

3.2. Conjugate heat transfer method

The CHT method is essential in multiphysics problems in which thermal interactions between solid and fluid domains are dominant. The solid and fluid domains are solved individually using separate solvers. The boundary values at the interface between the solid and fluid are then exchanged to couple the solid and fluid solvers. At the interface, the temperature and heat flux should be equal on both sides, which can be stated as follows:

$$T_f = T_s, \tag{9}$$

$$q''_f = q''_s. \tag{10}$$

There are two methods for solving a CHT problem: strong and weak coupling. In the strong coupling method, the solid and fluid domains are solved simultaneously. This approach shows a faster convergence, but it needs specific code development. On the other hand, in the weak coupling method, the solid and fluid domains are solved sequentially. This has the advantage of a modular approach, but it results in slower convergence than the strong coupling approach. The performance of the weak coupling technique greatly depends on the stability and accuracy of the coupling strategy followed at the interface.

In the weak coupling method, two different coupling approaches are available: loosely and tightly coupled, shown schematically in Fig. 4. In the loosely coupled approach, information exchange between solvers is performed once per time step, and the coupling time step should be decreased to avoid numerical instabilities. Even if the solvers are second-order accurate in time, the temporal accuracy of this approach is of the first order [46].

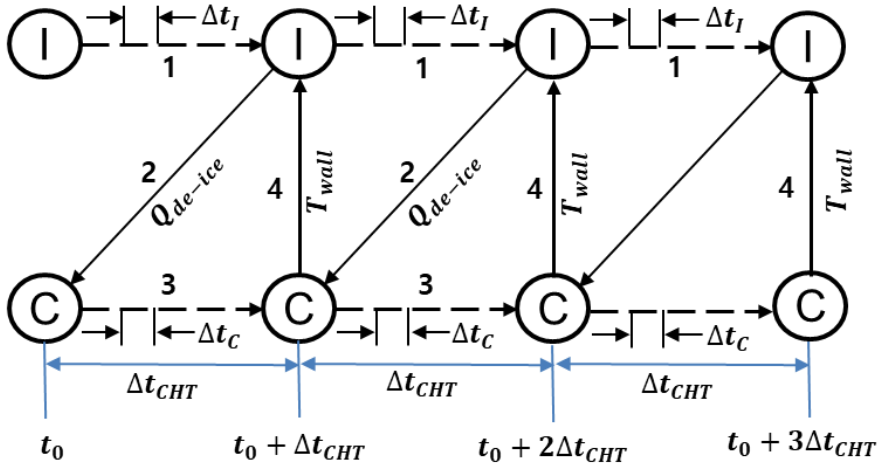

(a)

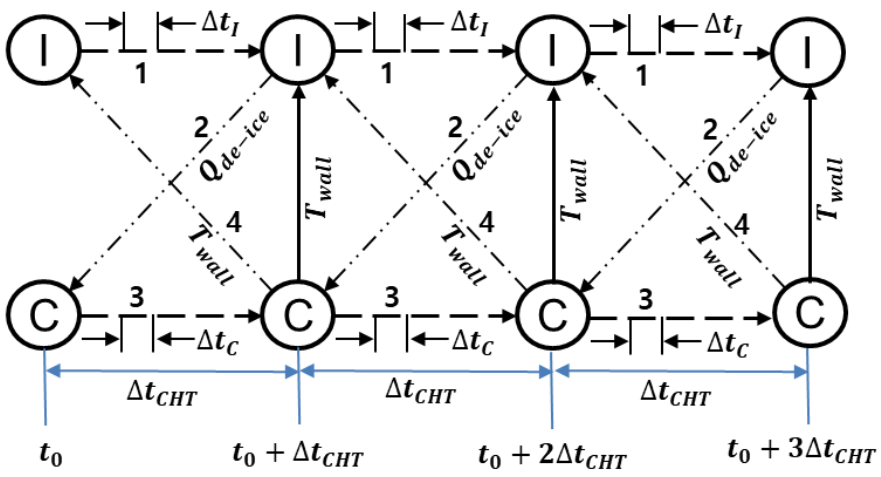

(b)

Fig. 4. (a) Loosely coupled and (b) tightly coupled approaches for the coupling of ice (I) and conduction (C) solvers.

In contrast, in the tightly coupled approach, sub-iterations are conducted at every CHT time step to achieve second-order temporal accuracy. Since the solid and fluid domains may have different time scales, the numerical time step of the solid and fluid solvers can be calculated independently based on their corresponding physical time scales. However, conducting a sub-iteration per time step in the tightly coupled approach can lead to numerical instabilities. To stabilize the tightly coupled method and accelerate its convergence, dynamic relaxation factors were employed to combine the current and previous solutions linearly.

The temperature in the present method is calculated using a post-processing approach as follows [47]:

$$T^{n+1} = (1-\omega^n)T^n + \omega^n \tilde{T}^{n+1}. \tag{11}$$

Here T^{n+1} and $\tilde{T}^{n+1}$ are the temperature after and before post-processing, respectively. Also, T^n and ω^n are the temperature in the previous solution and dynamic relaxation factor, respectively. The dynamic relaxation factor is calculated for every cell and in every time step using the following relations [47],

$$\omega^n = -\omega^{n-1}\frac{R^n}{R^{n+1}-R^n}, \tag{12}$$

$$R^{n+1} = \tilde{T}^{n+1} - T^n. \tag{13}$$

Sub-iterations per time step can be defined as a pre-defined number (explicit coupling) or based on a convergence criterion (implicit coupling). In explicit coupling, the continuity of the temperature and heat flux at the interfaces is not guaranteed, leading to numerical instabilities. On the other hand, in implicit coupling, the convergence criteria may never be fulfilled in a fair number of time steps. Consequently, a combination of convergence criteria and a maximum number of sub-iterations is used in the solver to circumvent these difficulties. Convergence criteria can be defined based on the relative or absolute error norms as follows,

$$\frac{\left\|R^{n+1}\right\|_{L^2}}{\left\|\tilde{T}^{n+1}\right\|_{L^2}} < \varepsilon_{rel}, \quad \left\|R^{n+1}\right\|_{L^2} < \varepsilon_{abs}. \tag{14}$$

This study describes the coupling between solid and fluid solvers using the partitioned method (weak coupling). The present solver was developed to be able to use both loosely and tightly coupled approaches. Depending on the physics, level of instability, desired accuracy, and computational time, we can decide to use a loosely/tightly coupled or implicit/explicit approach. For example, in the de-icing case, sub-iterations are employed between solvers, and coupled iterations are performed until a prescribed convergence tolerance.

3.3. Unsteady formulation of ice accretion/melting and runback water

The original SWIM model is a PDE-based thermodynamic method mainly developed for ice accretion applications, and it has limited ability to accurately describe unsteady de-icing processes. First, it was developed based on the adiabatic wall assumption, which overpredicts the equilibrium temperature at the surface. That is, the latent heat of fusion due to ice accretion can only be dissipated through the air [48], neglecting the conductive heat transfer to the substrate [49, 50]. Second, it can only predict the wall temperature in the equilibrium state. For example, in glaze icing conditions, the wall temperature at the leading edge reaches melting temperature from the first iteration. However, the

temperature in the solid is equal to the free-stream temperature, which is less than 273.15K. For an accurate CHT simulation, the temperature at the solid and ice interface should be equal; otherwise, the results are not converged at every CHT time step.

Two modifications were introduced to the SWIM model to develop an unsteady formulation for phase change and runback water. First, the temperature is considered to be a known quantity in the ice solver. Second, the phase change is assumed to occur in an artificial temperature range near the melting temperature, which enables the unsteady freezing fraction to be used to calculate the phase change rate.

In the new unsteady SWIM model, the unknowns are water film thickness (h_f), ice mass growth rate ($\dot{m}_{ice}$), and heat load ($\dot{Q}_{de-ice}$). Since we have two equations and three unknowns, compatibility relations are required to close the system of equations. The compatibility relations were also modified based on the new formulation, which can be expressed as follows:

$$\begin{aligned} &h_f \geq 0, \\ &M_{tot,ice} \geq 0, \\ &h_f T_{equi} \geq h_f T_{cr}, \\ &\dot{m}_{ice} T_{equi} \leq \dot{m}_{ice} T_{cr}. \end{aligned} \tag{15}$$

The first compatibility relation guarantees positive water film thickness. The second one ensures a positive total mass of ice in every cell. Previously, this compatibility relation was $\dot{m}_{ice} \geq 0$ to prevent the melting of the accumulated ice. However, ice melting occurs in de-icing, significantly affecting mass and energy conservation. The third one ensures that the water film can only exist at equilibrium temperatures above its freezing point. The last compatibility relation asserts that ice cannot form at equilibrium temperatures higher than the freezing point. For the third and fourth compatibility relations, the only difference between the original and modified compatibility relations comes from the definition of freezing point. In the original ice solver the phase change is assumed to occur at the critical temperature. However, in the new ice solver, we assume that it occurs in a small artificial temperature

range around the critical temperature. Based on this assumption, we introduce the freezing fraction rate, which allows us to calculate ice accretion and melting rate in a linear relationship with temperature.

The icing domain is divided into three regions using compatibility relations. These relations reduce the unknowns from three to two for each region. The first region corresponds to running wet with no ice accretion, described as $\dot{m}_{ice} = 0,\ h_f \geq 0$ and $T_{equi} \geq T_{cr} + \Delta T$. In this region, the unknowns are water film thickness and heat load, which can be calculated based on the mass and energy conservation equations. The second region is the glaze ice growth, where ice growth and water film coexist, represented by $M_{tot,ice} \geq 0,\ h_f \geq 0$ and $T_{cr} \leq T_{equi} \leq T_{cr} + \Delta T$. Finally, the third region corresponds to the rime ice case in which all impinging supercooled water droplets freeze, and no runback water exists in the region, expressed as $h_f = 0,\ \dot{m}_{ice} \geq 0$ and $T_{equi} < T_{cr}$. The algorithm of the new ice solver is summarized in Fig. 5.

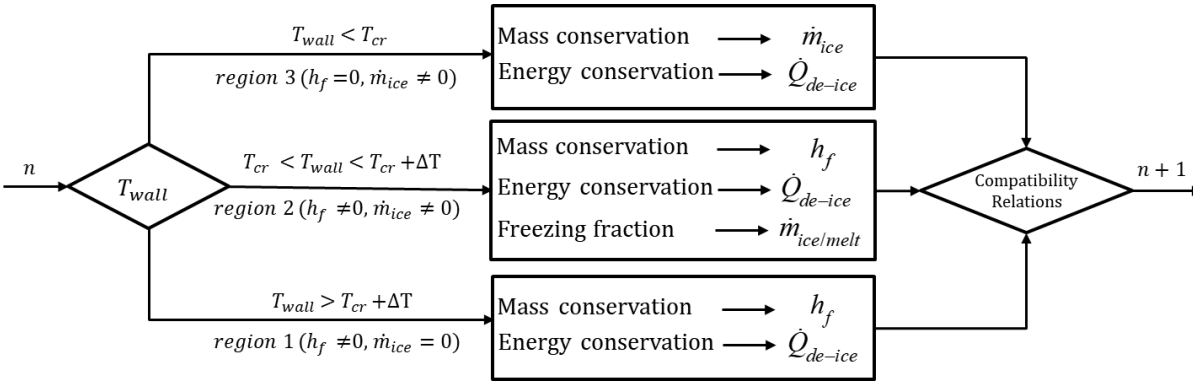

Fig. 5. The algorithm of the new ice solver.

In de-icing applications, ice accretion (due to impingement of supercooled water droplets) and ice melting (at ice/solid interface) can occur simultaneously. Consequently, the whole system of ice and water on the substrate can be divided into three control volumes consisting of water film (CV1), ice layer (CV2), and melted water (CV3) which are illustrated schematically in Fig. 6.

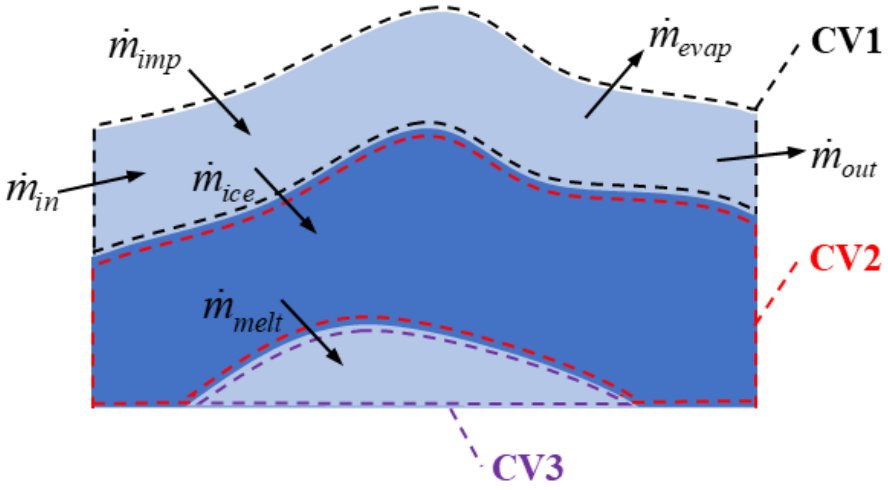

Fig. 6. Schematic of a typical system of ice and water in region 2.

The mass conservation equations for the water film, melted water, and ice layer can be expressed as follows, respectively,

$$\rho_w \frac{dh_f}{dt} + \dot{m}_{ice} = \dot{m}_{imp} - \dot{m}_{run} - \dot{m}_{evap}, \tag{16}$$

$$\rho_w \frac{dh_s}{dt} = -\dot{m}_{melt}, \tag{17}$$

$$\frac{dM_{ice}}{dt} = \dot{m}_{ice} + \dot{m}_{melt}, \tag{18}$$

where h_s, $\dot{m}_{melt}$, $\dot{m}_{run}$ and M_{ice} are the height of the melted water, ice melting rate, water mass flux, and mass of ice, respectively. In the ice accretion process, $\dot{m}_{ice}$ will be removed from the water film and added to the ice layer. In the ice melting process, the $\dot{m}_{melt}$ will be removed from the ice layer and added to the melted water. Since it is assumed that the ice melting occurs at the ice/substrate interface, the melted water is entrapped beneath the ice layer, and it thus does not contribute to the water film.

The second region in the ice solver requires special consideration in a de-icing simulation because there are four unknowns: water film thickness, ice accretion rate, melting rate, and heat load. In addition to the mass and energy conservation equations, we need two extra equations to calculate the phase change rates. The phase change was assumed to occur in an artificial temperature range (ΔT_{pc}) around

the melting temperature. This modification led to a linear relationship between the temperature and enthalpy in the phase change region. Moreover, an unsteady freezing fraction rate was introduced to calculate the ice accretion rate. Similarly, an unsteady mass fraction rate can be introduced to calculate the ice melting rate. Both the freezing fraction and mass rates have a linear relationship with temperature in the phase change region, resulting in two additional equations to close the system of equations.

Freezing fraction rate (f_{rate})

The ratio of ice accretion rate to the summation of ice accretion and water accumulation rate, f_{rate}, is introduced to measure what percentage of water entering the control volume is frozen, as follows,

$$f_{rate} = \frac{\text{ice accretion rate}}{\text{ice accretion rate + water accumulation rate}}. \tag{19}$$

By this definition, f_{rate} shows a continuous distribution through all cells, even if they belong to different regions. At $T \le T_{cr}$, all water entering the control volume is frozen, which means that there is no water accumulation in the cell, and the freezing fraction equals one. At $T \ge T_{cr} + \Delta T$, there is no ice accretion, resulting in zero freezing fraction. In the intermediate temperature range $T_{cr} \le T \le T_{cr} + \Delta T$, the freezing fraction value varies from one to zero, which is linearly related to temperature.

The mass conservation equation (16) can be rewritten as follows,

$$\dot{m}_{ice} + \rho_w \frac{dh_f}{dt} = \dot{m}_{imp} - \dot{m}_{run} - \dot{m}_{evap}, \tag{20}$$

where the second term on the left-hand side is the water accumulation rate. Consequently, the freezing fraction rate (19) can be written as follows,

$$f_{rate} = \frac{\dot{m}_{ice}}{\dot{m}_{imp} - \dot{m}_{run} - \dot{m}_{evap}}. \tag{21}$$

Mass fraction rate (f_{mass})

A mass fraction rate, f_{mass}, is introduced to include the accumulated ice layer in the mass and energy conservation equations,

$$f_{mass} = \frac{\text{total mass of ice in the control volume}}{\text{total mass of ice and melted water in the control volume}}, \quad (22)$$

ensuring that the total mass of ice is melted before the solver switches to region 1 (running wet with no ice accretion). Ice melting absorbs the latent heat of fusion, affecting the heat balance of the system. Here f_{mass} also shows a continuous distribution over all cells. At $T \le T_{cr}$, there is no melted water in the control volume (f_{mass}=1). At $T \ge T_{cr} + \Delta T$, there is no ice in the control volume (f_{mass}=0).

Considering $\frac{dM_{ice}}{dt} = \frac{M_{ice}^{n+1} - M_{ice}^{n}}{\Delta t}$, the mass conservation equation can be written as follows,

$$\frac{M_{ice}^{n+1} - M_{ice}^{n}}{\Delta t} = \dot{m}_{ice} + \dot{m}_{melt}, \quad (23)$$

equivalently,

$$M_{ice}^{n+1} - \Delta t \times \dot{m}_{melt} = M_{ice}^{n} + \Delta t \times \dot{m}_{ice}. \quad (24)$$

The first and second terms on the left-hand side are the mass of ice and mass of melted water in the control volume, respectively. The final form of mass fraction rate is reduced to

$$f_{mass} = \frac{M_{ice}^{n+1}}{M_{ice}^{n} + \Delta t \times \dot{m}_{ice}}. \quad (25)$$

Furthermore, the freezing fraction can be defined as a linear function of temperature throughout the phase change temperature range, ΔT_{pc},

$$f = 1 - \frac{T - T_{cr}}{\Delta T_{pc}}. \quad (26)$$

Based on this definition, the freezing fraction decreases linearly for the temperature from one at $T = T_{cr}$ to zero at $T = T_{cr} + \Delta T_{pc}$. Combining equations (21) and (26), we can derive a new equation to calculate $\dot{m}_{ice}$ in region 2 (glaze ice growth),

$$\dot{m}_{ice} = f(\dot{m}_{imp} - \dot{m}_{run} - \dot{m}_{evap}). \quad (27)$$

Similarly, by combining equations (25) and (26), we can derive an equation for the calculation of the total mass of ice in region 2 (glaze ice growth) as follows,

$$M_{ice}^{n+1} = f\,(M_{ice}^{n} + \Delta t \times \dot{m}_{ice}). \tag{28}$$

Substituting equation (28) into equation (18), we can derive the following relation to predict the melting rate,

$$\dot{m}_{melt} = (f - 1)(\frac{M_{ice}^{n}}{\Delta t} + \dot{m}_{ice}). \tag{29}$$

4. Unsteady simulation of electrothermal de-icing process and discussion

The unsteady simulation of de-icing of in-flight aircraft icing is a multiphysics problem that requires different physics-based solvers to capture adequate physics in the different domains of interest. The different solvers need to be accurate individually and coupled efficiently to carry out a successful simulation. The airflow, droplet impingement, and original ice accretion solver were verified successfully in previous works [41, 42]. Only the verification of the heat conduction solver and the validation of the electrothermal de-icing solver are presented here.

4.1. Verification of heat conduction solver

A comprehensive verification study was conducted to evaluate the order of accuracy of the heat conduction solver. However, only the verification study of a one-dimensional composite slab (example 8-4 of Ref. [51]) is presented here for simplicity. The slab consists of two layers with different thermal properties that are in perfect thermal contact. The thermal conductivities and diffusivities of the first ($0<x<a$) and second layers ($a<x<b$) are k_1, k_2, α_1, and α_2. Initial conditions are set as follows,

$$\begin{aligned} T_1(x, t=0) &= T_1, \\ T_2(x, t=0) &= T_2. \end{aligned} \tag{30}$$

Boundary conditions are assumed as follows,

$$
\begin{aligned}
&T_1(x=0,t)=0,\\
&T_1(x=a,t)=T_2(x=a,t),\\
&k_1\frac{\partial T_1}{\partial x}=k_2\frac{\partial T_2}{\partial x};\ x=a,\ t>0,\\
&k_2\frac{\partial T_2}{\partial x}+h(T_2-T_\infty);\ x=b,\ t>0.
\end{aligned}
\tag{31}
$$

The first condition denotes the Dirichlet condition at x=0, the second and third one stands for the continuity of temperature and heat flux at the interface of the two layers, respectively, and the last one denotes the convective boundary condition at x=b.

Fig. 7 shows the error norms (left) and a comparison of the temperature profile through the slab for the numerical and analytical solutions (right). The numerical results show the second-order accuracy of the heat conduction solver and are in very good agreement with the analytical solutions.

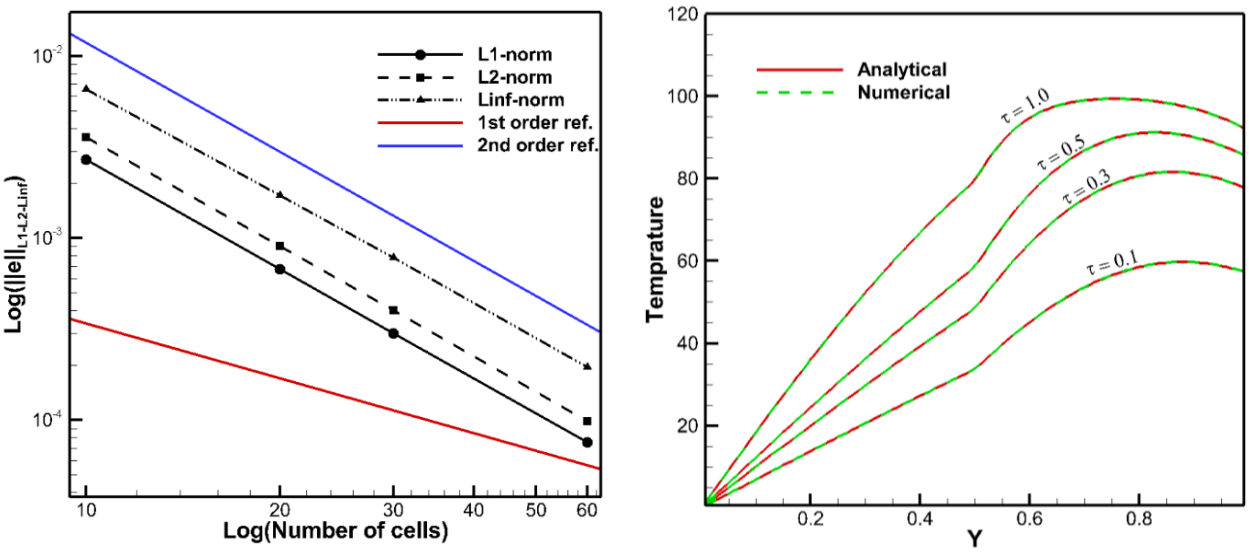

Fig. 7. Error norms (left) and temperature profile along the slab (right).

4.2. Validation of electrothermal de-icing solver

To validate the unsteady de-icing solver, we chose electrothermal de-icing experiments conducted in the NASA Lewis Icing Research Tunnel [52]. The wing section profile is NACA0012 with a chord length of 0.9144m. The leading edge consists of a 6-layer composite in which seven heater pads are

implemented as the ice protection system. The positions of the heaters on the leading edge, and a cross-section of the leading edge illustrating the materials in the multilayer structure, are shown in Fig. 8. The computational domain consists of a solid and a fluid grid, as shown in Fig. 9. Both the solid and fluid grids are fully structured. The height of the first cell in the fluid grid is small enough to have $y^+<1$, ensuring an accurate prediction of shear stress and convective heat transfer coefficient at the wall.

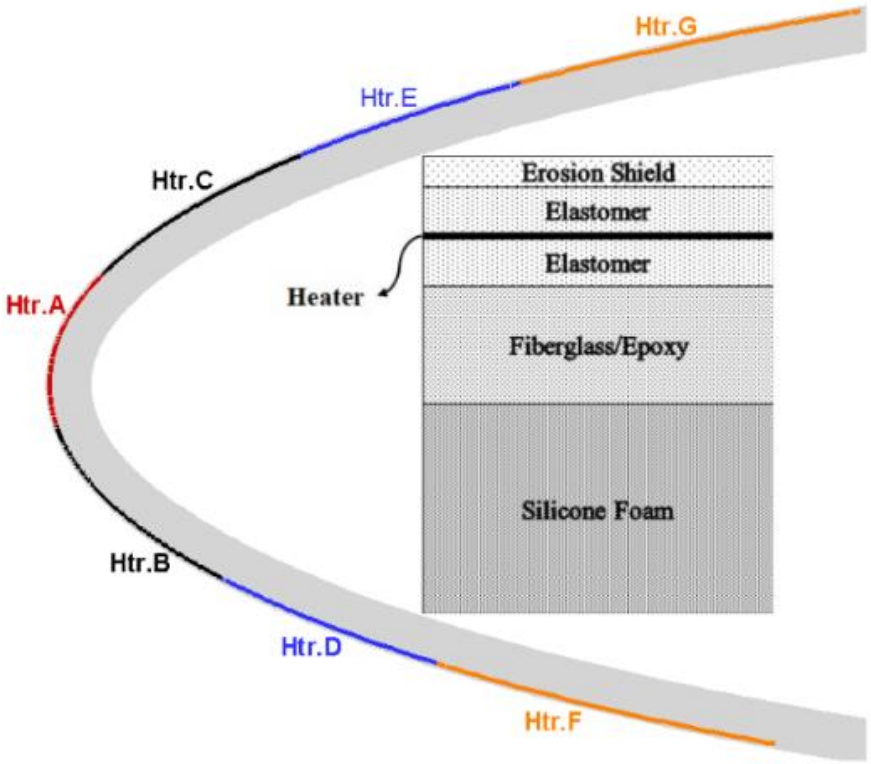

Fig. 8. Composite layering and arrangement of heaters.

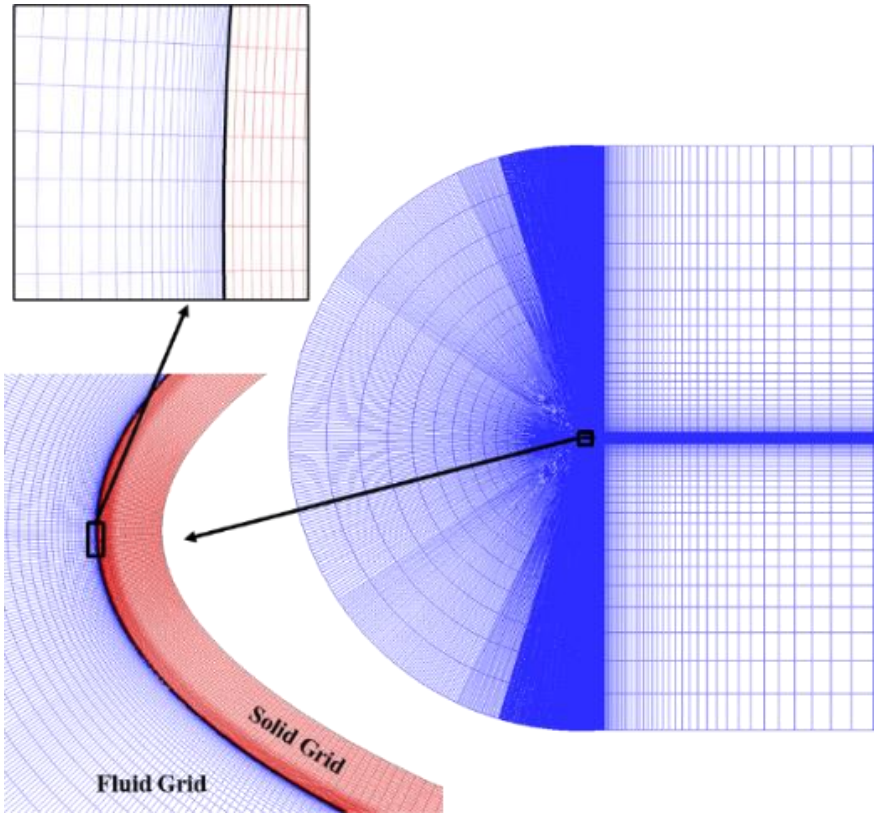

Fig. 9. Computational domain consisting of solid and fluid grids.

The leading edge consists of an erosion shield layer, two elastomer layers, a fiberglass/epoxy layer, and a silicone foam layer. The heater pads were placed between two layers of elastomer to distribute heat homogeneously. The fiberglass/epoxy and foam layers have low conductivity, to avoid heat leakage to the wing's inner structure. The thermal properties of the different layers are tabulated in Table 2.

Table 2
Material properties of the composite layers.

Material	Thickness [mm]	ρ [kg/m^3]	k [W/m·K]	C_p [J/Kg·K]
Heating Element	0.013 (x1)	8906.3	41	385
Erosion Shield	0.203 (x1)	8025.3	16.3	502
Elastomer	0.280 (x2)	1383.9	0.256	1260
Fiberglass/Epoxy Composite	0.890 (x1)	1794.0	0.294	1570
Silicon Foam Insulation	3.430 (x1)	648.8	0.121	1130

It is worth mentioning that all heater pads were shifted by 4.7625mm toward the upper side of the airfoil, leading to a non-symmetric arrangement of heaters pads over the leading edge. Each de-icing

cycle takes 120s to be completed. Heater A is always turned on during the simulation, heaters B and C are turned on from 100s to 110s, and heaters D-G are turned on from 110s to 120s. There is no accumulated ice layer at the beginning of the simulation because the heater cycle sequence and water spray bars start simultaneously. The atmospheric and icing conditions of the two validation cases as well as the corresponding heater power densities are summarized in Table 3.

Table 3
Heater powers and icing conditions for the validation cases.

variables	Case 1	Case 2
Heater A [W/m^2]	7750	7750
Heater B-C [W/m^2]	15500	10850
Heater D-G [W/m^2]	12400	10850
T_∞ [K]	266.483	266.483
U_∞ [m/s]	44.704	44.704
LWC [g/m^3]	0.78	0.78
MVD [μm]	20	20

Convective heat transfer plays an important role in the conservation of mass and energy in the ice solver. Fig. 10 compares the convective heat transfer coefficients calculated by the present solver with previous data. Present results show acceptable agreement with LEWICE results [53].

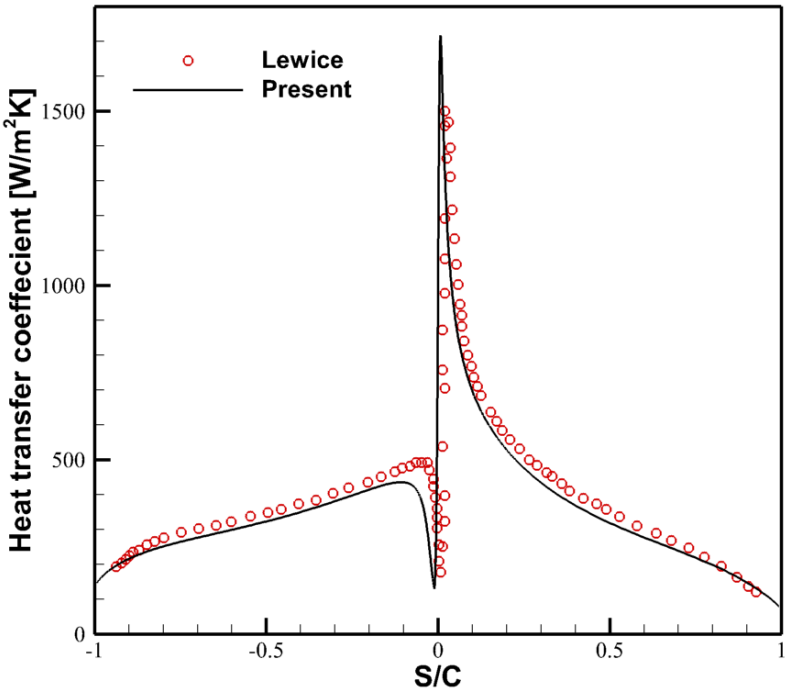

Fig. 10. Convective heat transfer coefficients over a NACA0012 airfoil at AOA = 4˚, M = 0.32 and T=262.04 K.

The CHT coupling time step (Δt_{CHT}) specifies the frequency of information exchange between individual solvers during the unsteady de-icing simulation. The numerical time step for solving the individual solvers (ice and heat conduction) is Δt=1e^{-4}. To verify the independence of the computational results to Δt_{CHT}, we conducted de-icing simulations with three different CHT time steps, of $\Delta t_{CHT}=\Delta t$, $10\Delta t$, and $100\Delta t$. Similarly, to verify the independence of computational results to ΔT_{pc}, we conducted de-icing simulations for various artificial temperature ranges as ΔT_{pc}=0.01, 0.05, 0.1, and 0.2. The results of both studies are shown in Fig. 11, demonstrating the independence of the numerical results to the CHT time step and artificial temperature range.

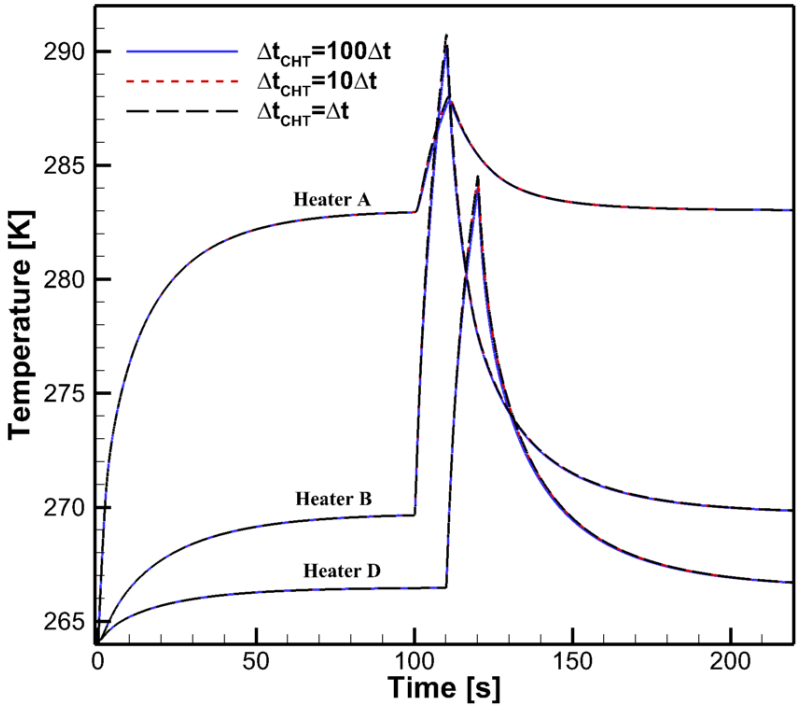

(a)

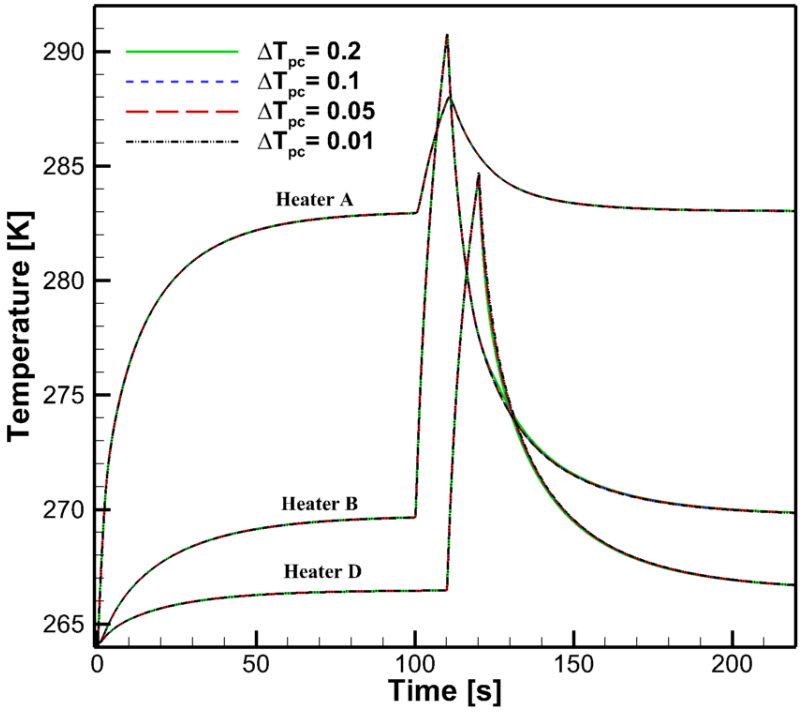

(b)

Fig. 11. Temperature variation over time for case 1 (a) for different CHT coupling time steps and (b) for various artificial temperature ranges.

Fig. 12 compares the temperature variations over time at heaters A, B, and D for cases 1 and 2 obtained by the current solver, using data (experiment, LEWICE, FENSAP) available in the literature. Overall, the present results show better agreement with the experimental data for both case 1 and case 2, compared to other results obtained by LEWICE and FENSAP. Atmospheric and icing conditions and the power density of heater A are the same for case 1 and case 2, and consequently, the first 100s of de-icing simulations are identical for both cases. The heater power densities for the other heaters are different, leading to different results for the rest of the simulation.

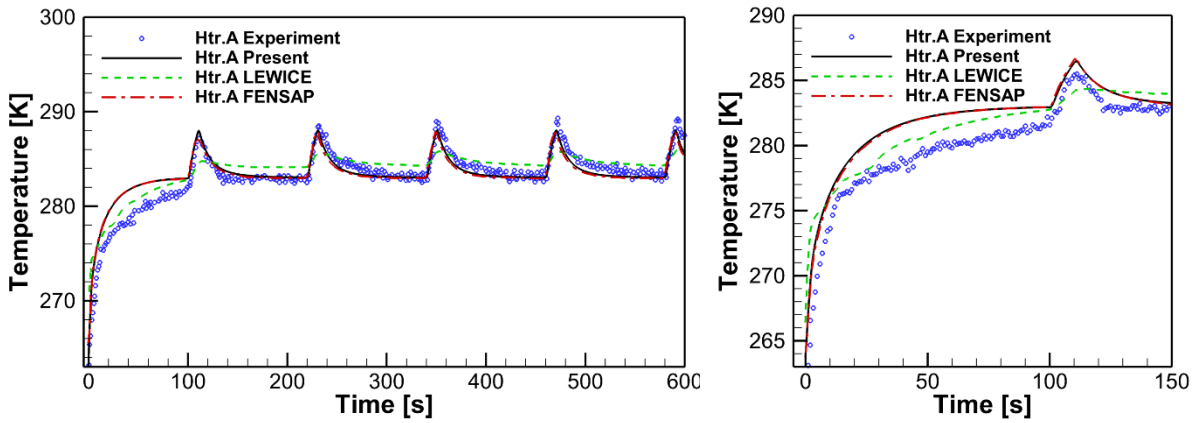

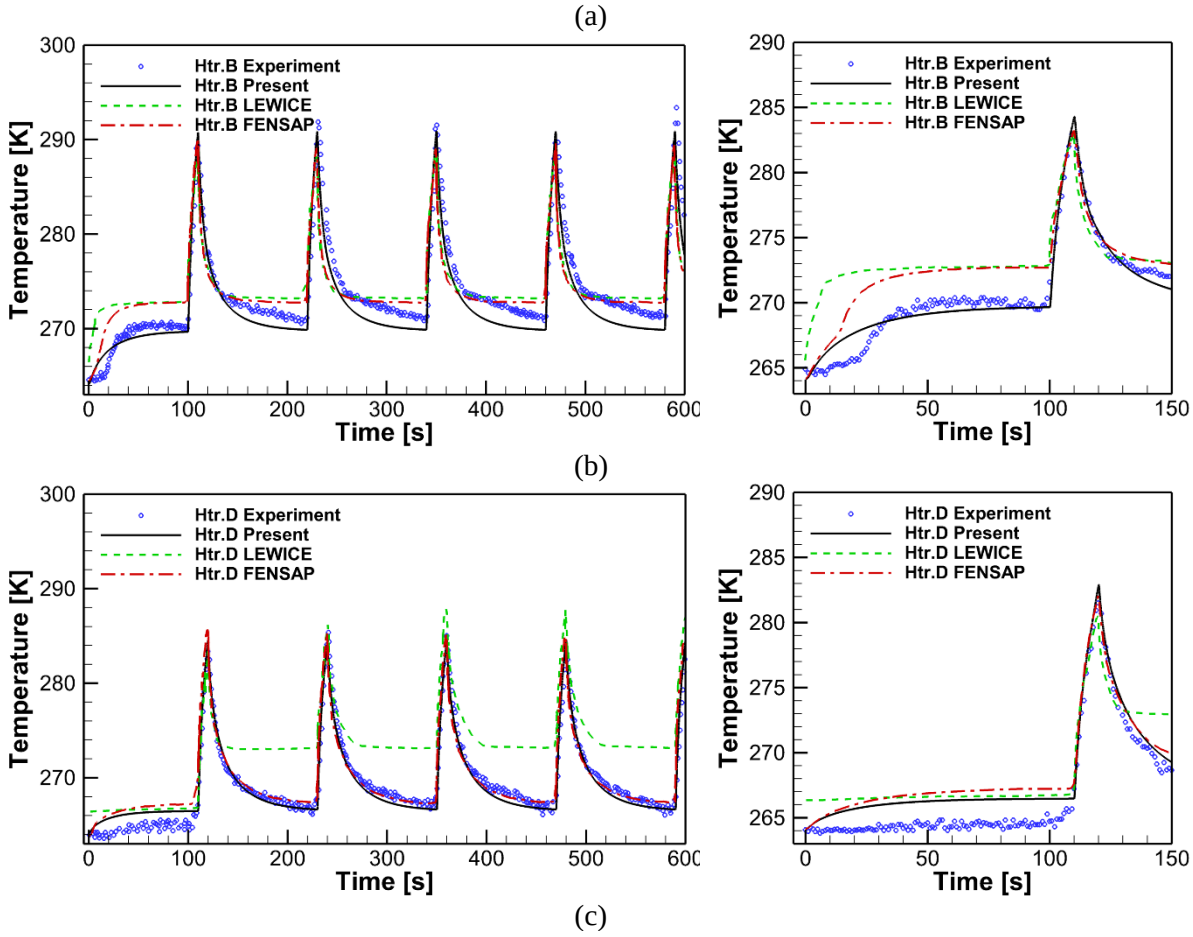

Fig. 12. Comparison of temperature variations over time at (a) heater A, (b) heater B, and (c) heater D for case 1 (left) and case 2 (right).

The surface temperature at zone A increased rapidly due to the combined effect of heat propagation from heater A and the release of latent heat of fusion (owing to the ice accretion). Once the surface temperature reaches the melting temperature, the accumulated ice layer melts and absorbs the latent heat of fusion. At the same time, some portion of the impinging supercooled water droplets does not freeze and run back as a thin water film, reducing the ice accretion rate. Consequently, the temperature at the surface remains almost constant, and the rate of temperature increase in the heater decreases as well. Only water exists on the leading edge once the total mass of ice is melted on the surface. Due to heat propagation from heater A to the surface, the water temperature will increase until a thermodynamic balance is reached between the heat supply from the heater and heat dissipation through evaporation and convection.

The temperature at heater A in the experimental data increased rapidly at first, then increased linearly at a lower rate up to t=100s. However, in the present results, the temperature asymptotically reaches an equilibrium temperature. This difference in temperature variation behavior between the experimental and numerical results was also found in the FENSAP results. One possible explanation for this gap is that the convective heat transfer coefficient in the airflow simulation is not updated based on the unsteady temperature distribution at the wall, affecting the heat balance at the surface. Another possibility is that we assumed perfect thermal contact between the different composite layers and also between the wing surface and the ice/water layer. However, a temperature jump can occur between the composite layers due to imperfect thermal contact. Furthermore, air trapped between the ice and surface can alter the thermal interaction characteristics of the wing surface and ice/water layer.

While the temperature at heater B increases asymptotically to 269K within 100s in the present results, it reaches 270K linearly in the experimental data. The present solver performed better than the LEWICE and FENSAP, which reached a much higher temperature, 273.15K. The difference in temperature predictions between the present and other computational results is probably due to the difference in the predictions of the water film extent on the surface. In general, ice accretion occurs from the top surface of the ice layer, whereas melting by a heater occurs from the bottom surface of the ice layer. Hence, in the present solver, it is assumed that the heat from the heater pad first melts the existing ice layer on the surface, and excess energy prevents further ice accretion. As a result, the heat from the substrate first melts the ice layer at the interface between the substrate and ice. When the ice layer is completely melted, the heater energy changes the thermal balance of the surface in a way that reduces the freezing fraction. The present solver predicted zone B would be covered by pure ice within 100 seconds, while FENSAP predicted zone B would be covered by a mixture of ice and water. According to the present results, the temperature at heater B cools to almost 269K in the cooling stage, which agrees with the experimental data. However, LEWICE and FENSAP predicted that the temperature would not cool below 273K. This difference may again come from the different predictions of water film extent.

Finally, the temperature variation at heater D showed excellent agreement with the experimental data. This zone is out of the impingement limit. Consequently, the present and FENSAP results were almost the same and both agreed well with the experimental results. On the other hand, LEWICE predicted that the temperature would not cool below 273K, leading to a large deviation from the experimental data.

Besides better agreement with the experimental results, the present solver performs better at computational time. A full cycle of the de-icing simulation was conducted on the same grid by the present solver and FENSAP. The results show that the computational time of the present solver accounts for about 20 percent of the computational time of the FENSAP. In the present solver, a single grid system is used for all submodules to bypass the interpolation process. Furthermore, the phase change and runback water are solved in the same solver, eliminating additional grid generation for the ice layer. On the other hand, in FENSAP, the ice layer is re-meshed at every CHT iteration, making it relatively computationally expensive.

Fig. 13 compares the surface temperature distributions over all zones at different times (105s, 110s, 115s, 120s) for the different solvers. Interestingly, despite comparing the 105-120s time period, where the difference between the three solvers was not expected to be very large as seen in Fig. 12, a considerable difference was observed in the detailed temperature distribution, implying the importance of having accurate physical and numerical modeling for the unsteady de-icing process.

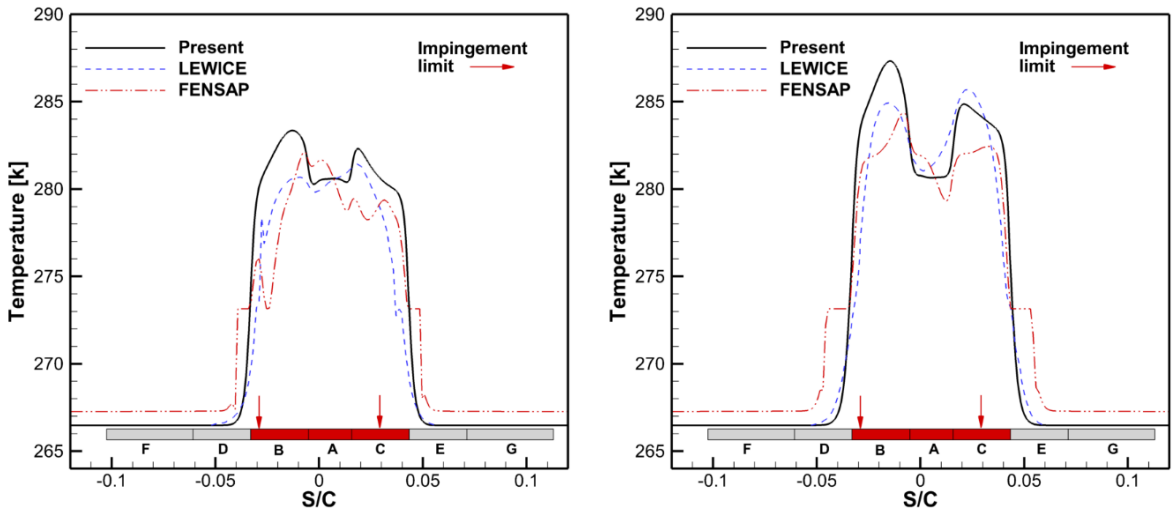

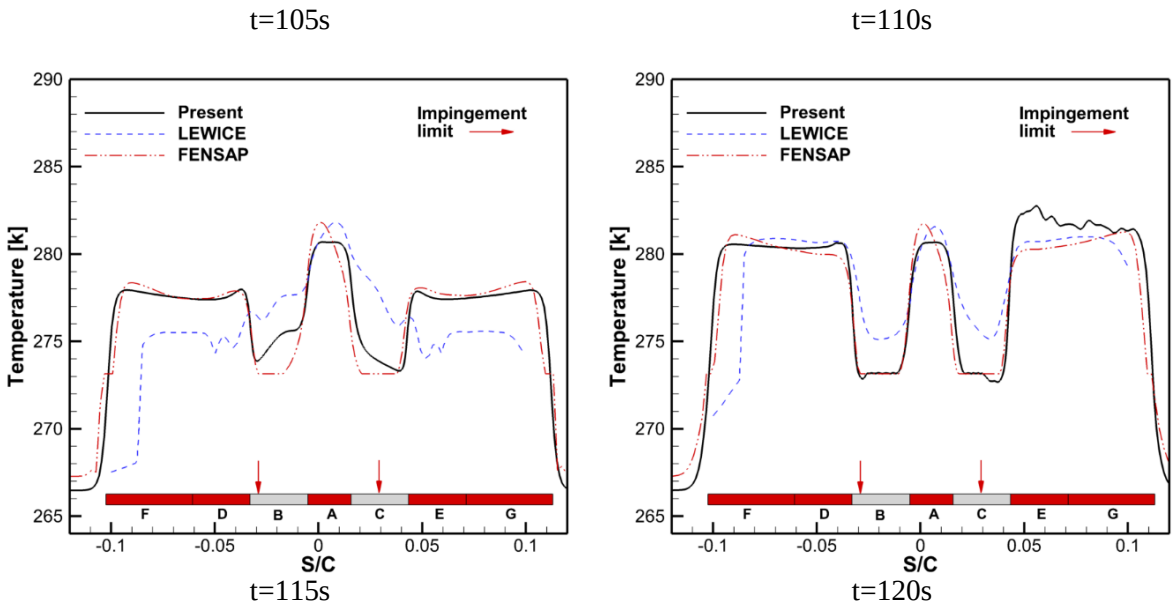

Fig. 13. Surface temperature at different times (105s, 110s, 115s, 120s) for case 1.

4.3. Analysis of the electrothermal de-icing process

Next, the unsteady process of the electrothermal de-icing was investigated: ice accretion, ice melting, water film dynamics, and water film freezing. In a typical electrothermal de-icing process, ice is accreted on the surface due to the impact of supercooled water droplets. Ice melting occurs due to the heat provided by the IPS and this may result in a flowing water film beyond the impingement limits. Moreover, the water film can freeze on unprotected areas out of the impingement limits, forming ice ridges. During the process, the heater pads were turned on and off sequentially, creating heating and cooling stages during the de-icing cycle.

Fig. 14 illustrates the complicated profiles of temperature, heat load, ice accretion rate, water film thickness, ice mass, and ice melting rate at different times from 1.4s to 4.9s. These results focus on region 2 of the ice solver, where the surface reaches the critical temperature. At t=1.4s, the temperature is lower than the critical temperature, and all incoming droplets freeze upon impact. Some portion of latent heat due to the ice accretion will be dissipated through the substrate, causing a positive heat load. As heat propagates toward the surface, temperature increases until it reaches the melting temperature, and the ice solver switches to region 2 (including the results of t=2, 3, 4, 4.5s). In this region, the

temperature varies over a small temperature range, reflecting the phase change process where the temperature is almost constant and enthalpy increases, as shown in Figs. 14a,b.

When temperature increases from T_{cr} to $T_{cr}+\Delta T$, the unsteady freezing fraction decreases from one to zero. As a result, $\dot{m}_{ice}$ decreases from equation (27). In the mass conservation equation (16), the $\dot{m}_{imp}$ and $\dot{m}_{evap}$ are almost constant. Consequently, the water film height increases while the ice accretion rate decreases, as shown in Figs. 14c,d. Once the ice accretion rate becomes zero, the water film height does not change anymore. When the surface temperature reaches the critical temperature, the ice accretion on the top of the ice layer and ice melting from beneath occur simultaneously. The net rate of ice accretion and melting rate will determine the total mass of ice in the system. At *t*=2s, the net rate of ice accretion and melting is positive, leading to an increase in ice mass. However, from *t*=3s, the net rate of accretion and melting is negative, leading to a decrease in ice mass, until all the ice melts at *t*=4.9s. Melting ice absorbs the latent heat of fusion, reducing the heat load to negative values. As a result, the surface is cooling due to melting, and the temperature remains almost constant (Figs. 14a,b). When the temperature exceeds $T_{cr}+\Delta T$, the ice solver switches to region 1, in which there is no ice on the surface to be melted. As a result, the heat load increases, causing a rapid increase in surface temperature.

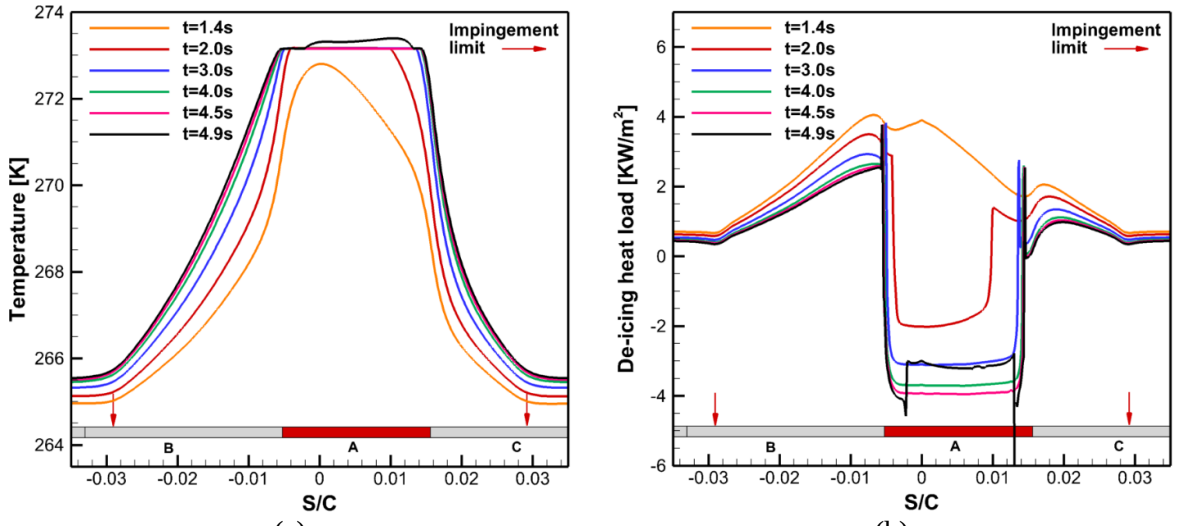

(a) (b)

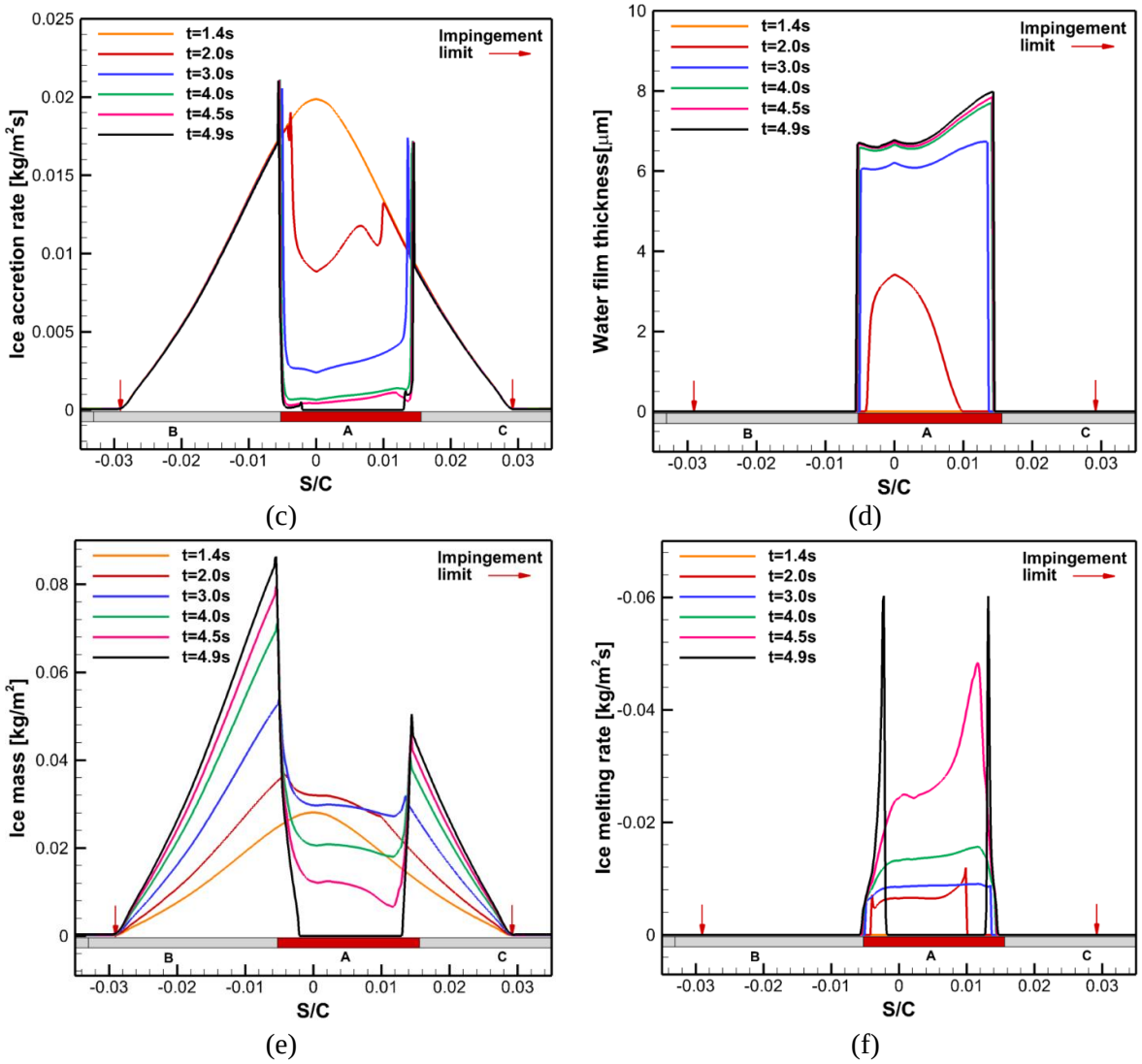

Fig. 14. Profiles at different times (1.4s to 4.9s) for case 1: (a) Temperature; (b) de-icing heat load; (c) ice accretion rate; (d) water film thickness; (e) ice mass; and (f) ice melting rate.

Fig. 15 illustrates profiles of the temperature, de-icing heat load, ice mass, and water film thickness from t=10s to t=100s when only heater A is turned on. Temperature profiles show an asymmetric behavior due to the asymmetric arrangement of heaters on the leading edge. At the pressure side of the airfoil, there is a flat region where the temperature profile has a constant value in the vicinity of the freezing temperature. This flat region corresponds to the glaze ice accretion, where only some portion of impinging water droplets freezes on the surface. When the temperature is greater than the critical temperature in zone A, there is no ice layer, and temperature increases asymptotically from t=10s to t=100s. During this period, heat is balanced at the surface, and the heat provided by heater A is almost equal to heat dissipation by convective heat transfer, with the result that temperature profiles do not

change much. However, when the temperature is equal to or less than the critical temperature in the zones around heaters B and C, the ice layer grows in these zones, as shown in Fig. 15c. Further, the release of latent heat of fusion warms the surface in the absence of heat from heaters, resulting in a positive heat load (Fig. 15b). The water film height remains almost constant with time in zone A, and only its extent grows slowly as heat is conducted in the chordwise direction (from A to B, C), warming the surface (Fig. 15d).

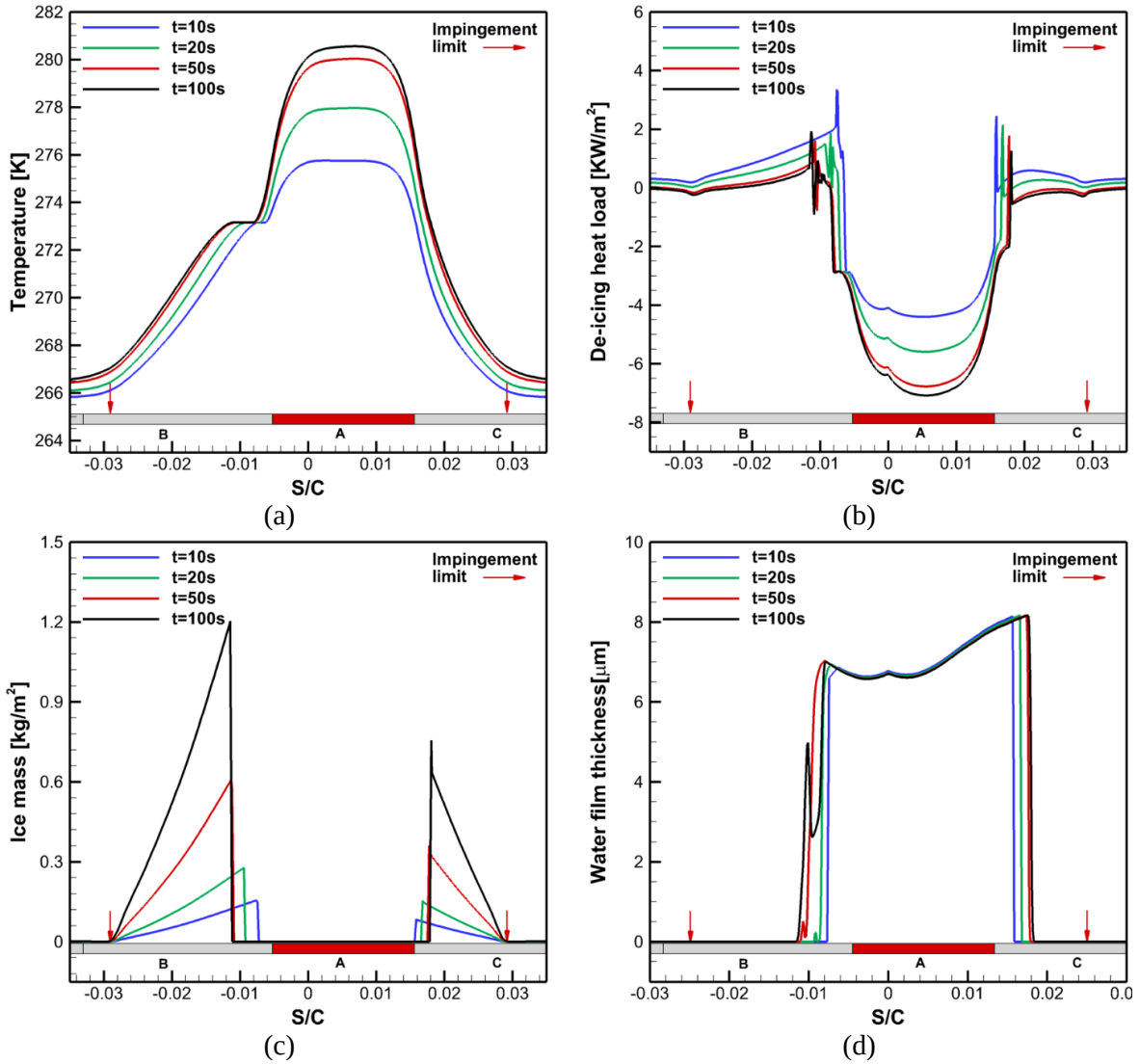

Fig. 15. Profiles at different times (10s to 100s) for case 1: (a) Temperature; (b) de-icing heat load; (c) ice mass; and (d) water film thickness.

Fig. 16 illustrates temperature contours inside the composite layers along with ice shape and water film on the airfoil surface from *t*=100s to *t*=220s for case 1. At *t*=100s, before turning on heaters B and C, water covers zone A, and some portions of zones B and C. The remaining portions of zones B and

C (in the impingement limit) are covered with ice. From *t*=100s to *t*=110s, heaters B and C are turned on, warming up zones B and C. Consequently, the temperature rises, ice melts, and water film runs back in the chordwise direction beyond the impingement limit, as shown in the case at *t*=110s. It is worth mentioning that we assume the water film fully wet the surface. However, continuous water film flow beyond the impingement limits can be split into rivulets or even isolated water droplets (beads) due to the water film instabilities [54].

When heaters B and C are turned off from t=110s, the surface in zones B and C cools down to freezing temperature at t=120s. At the same time, because the remaining heaters are turned on from t=110s to t=120s, water film flows downstream all over zones D, E, F, and G, reaching its most extensive range on the surface at t=115s. Since water film reaches the unprotected area beyond the heater regions of F and G, it freezes, and an ice ridge forms. De-icing helps to melt the ice on the leading edge of the airfoil and move water to less critical areas of the airfoil, but the ice ridge height increases after each de-icing cycle. If the ice ridge exceeds a considerable size, it can increase drag and results in flow separation. From t=115s to t=120s, the water film gradually disappears from the surface (due to evaporation) except for the impingement limit area. Since all heaters except heater A are turned off, the surface temperature decreases from 120s to 220s, and ice again accumulates in zones B and C.

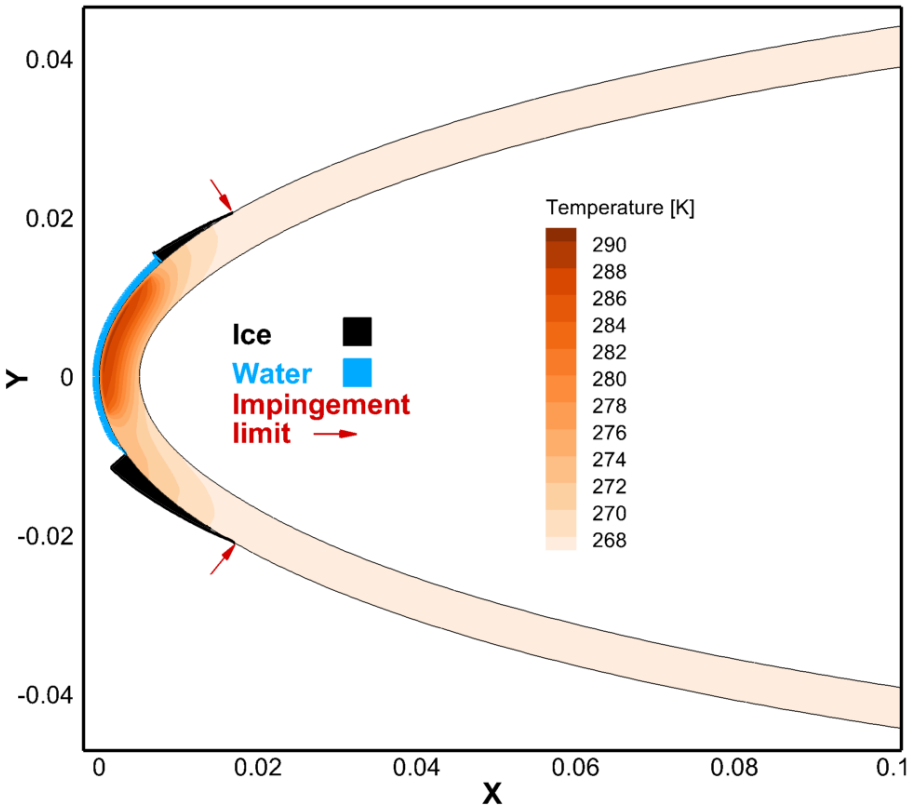
0.04
0.02
0
-0.02
-0.04
Y
0
0.02
0.04
0.06
0.08
0.1
X
Ice
Water
Impingement
limit
Temperature [K]
290
288
286
284
282
280
278
276
274
272
270
268

t=100s

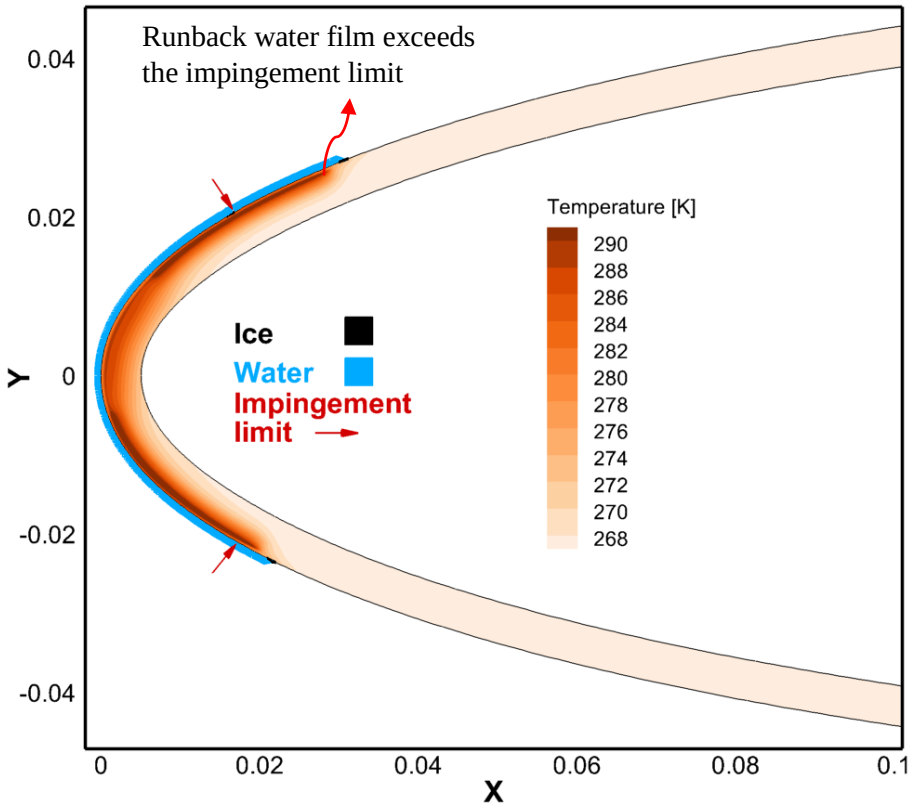
Runback water film exceeds
the impingement limit
0.04
0.02
0
-0.02
-0.04
Y
0
0.02
0.04
0.06
0.08
0.1
X
Ice
Water
Impingement
limit
Temperature [K]
290
288
286
284
282
280
278
276
274
272
270
268

t=110s

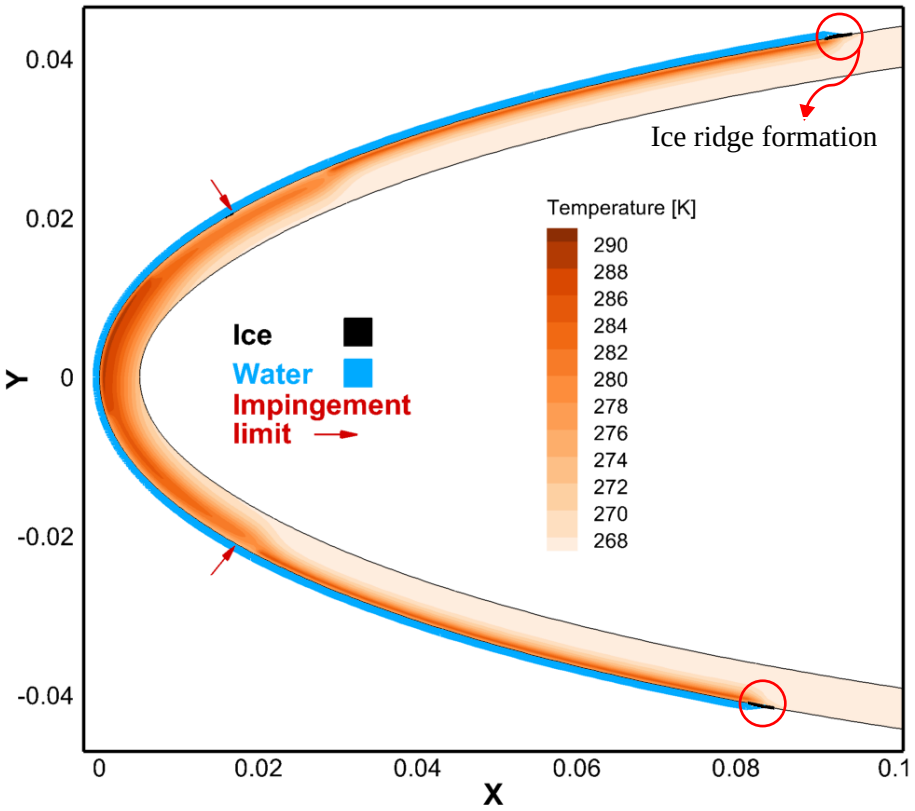
Ice ridge formation
Temperature [K]
290
288
286
284
282
280
278
276
274
272
270
268
Ice
Water
Impingement
limit
0.04
0.02
0
-0.02
-0.04
Y
0
0.02
0.04
0.06
0.08
0.1
X

t=115s

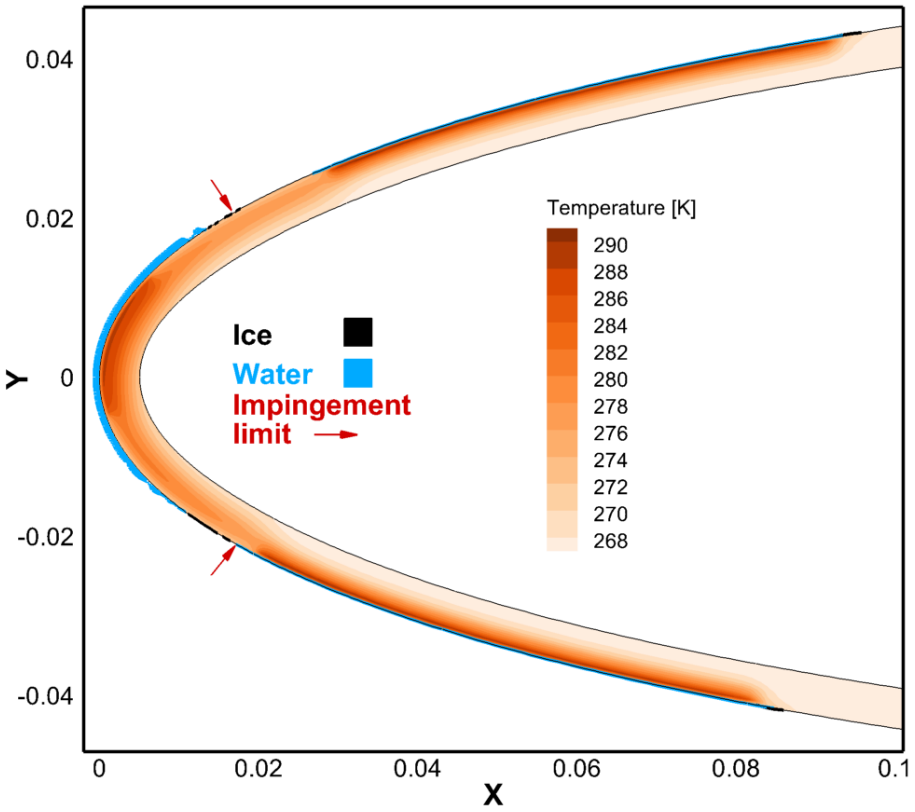
Temperature [K]
290
288
286
284
282
280
278
276
274
272
270
268
Ice
Water
Impingement
limit
0.04
0.02
0
-0.02
-0.04
Y
0
0.02
0.04
0.06
0.08
0.1
X

t=120s

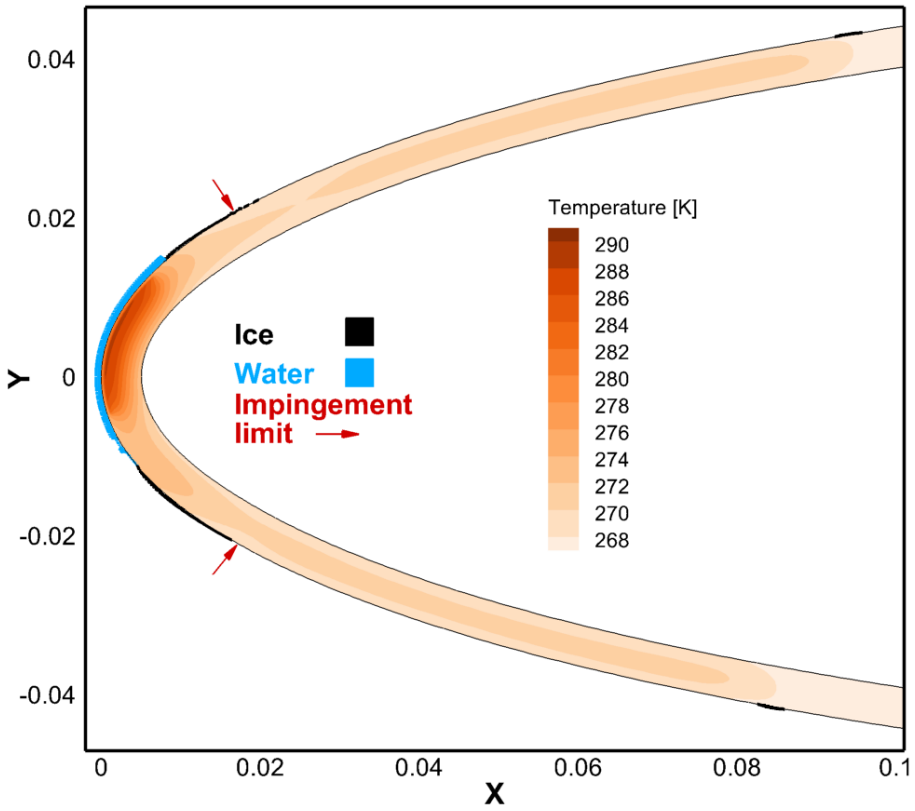
0.04
0.02
0
-0.02
-0.04
Y
0
0.02
0.04
0.06
0.08
0.1
X
Ice
Water
Impingement
limit
Temperature [K]
290
288
286
284
282
280
278
276
274
272
270
268

t=150s

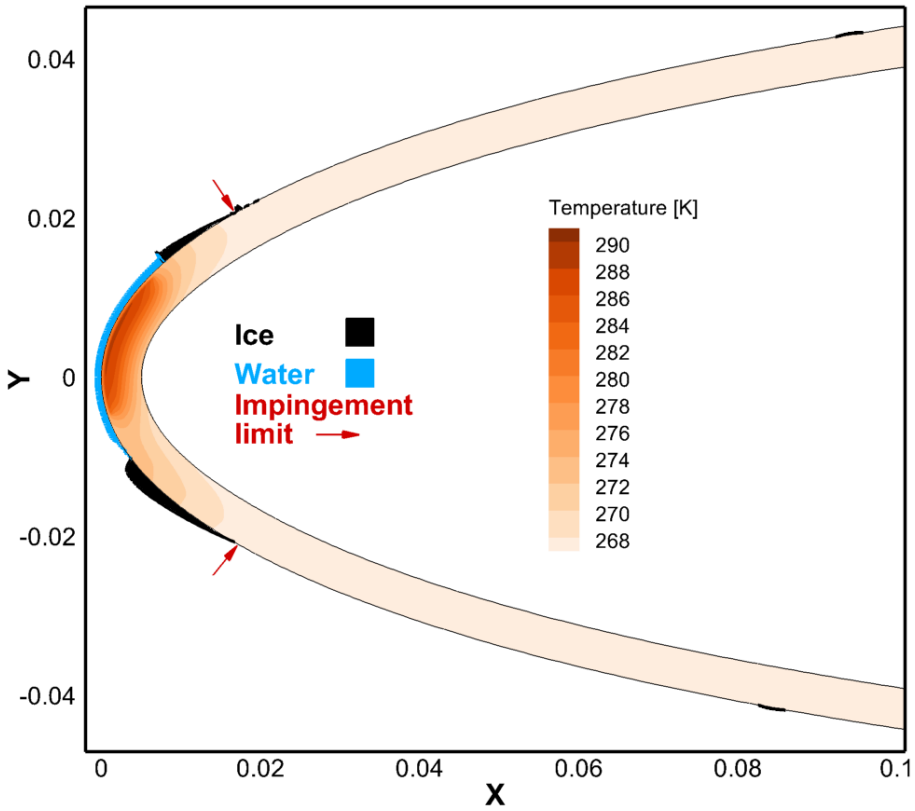
0.04
0.02
0
-0.02
-0.04
Y
0
0.02
0.04
0.06
0.08
0.1
X
Ice
Water
Impingement
limit
Temperature [K]
290
288
286
284
282
280
278
276
274
272
270
268

t=220s

Fig. 16. Ice shape, water film, and temperature contours at different times for case 1. (For visualization purposes, ice height and water film were scaled up 2 times and 100 times, respectively).

5. Conclusions

A computational CHT solver for the electrothermal de-icing (ice accretion/melting) process in atmospheric icing was developed, based on an unsteady formulation of phase change and runback water. The unsteady ice model predicts ice accretion/melting and runback water in a unified FVM framework, removing the need for any extra grid generation for the narrow ice layer. A CHT method was developed to tightly couple the ice and heat conduction solvers during the unsteady electrothermal de-icing process. Sub-iterations are performed in every CHT iteration to guarantee the convergence of temperature and heat flux at the interface. A dynamic relaxation factor was also introduced to stabilize the tightly coupled method and accelerate its convergence in the CHT sub-iterations.

The unsteady electrothermal de-icing solver consists of a compressible Navier-Stokes-Fourier airflow solver, an Eulerian droplet impingement solver, an unsteady ice accretion/melting solver, and a heat conduction solver, which can handle multilayer composite materials. Since all of the solvers were developed in the same FVM framework based on a single grid system, all the information can be efficiently transferred between the different solvers without losing data in the interpolation process that occurs when transferring data from one grid to another.

Two physically-motivated concepts were newly introduced to the icing model to accurately describe the unsteady electrothermal de-icing (ice accretion/melting) process, which is dominated by phase change and runback water. The temperature at the surface was considered to be a known quantity in the ice solver, in contrast with previous ice solvers. In the new icing model, there can be four unknowns in a region: water film thickness, ice accretion rate, melting rate, and heat load. In addition, a phase change was assumed to occur in an artificial temperature range near the melting temperature, which enables the unsteady freezing fraction to be used to calculate the phase change rate.

Overall, the present results showed better agreement with experimental data, compared to other computational results. An in-depth analysis of the electrothermal de-icing process was also conducted

by investigating ice accretion, ice melting, water film dynamics, and water film freezing in unprotected areas with time. The analysis showed that the water film could run back beyond the impingement limits and freeze in unprotected areas resulting in ice ridge formation. Further, ice accretion and melting rates were predicted independently, using the unsteady freezing fraction and mass fraction rate, respectively. This enabled us to simultaneously simulate ice accretion on the top of the ice layer and ice melting from beneath, which is characteristic of the new solver.

In this study, the airflow simulation results remained unchanged during the unsteady de-icing simulation. The convective heat transfer coefficient was thus not updated based on unsteady temperature distribution at the wall. In a future study, we plan to tightly couple the airflow solver in the electrothermal de-icing framework to utilize the unsteady convective heat transfer coefficient, and wall shear stress, in the mass and heat balance of the ice solver. It will also be of great interest to consider the effect of surface wettability on droplet impingement and water film dynamics.

Acknowledgment

This work was supported by the National Research Foundation of Korea (NRF) Grant funded by the Ministry of Science and ICT (NRF-2017-R1A5A1015311), South Korea.

References

[1] R.W. Gent, N.P. Dart, J.T. Cansdale, Aircraft icing, Philos. Trans. R. Soc. London, Ser. A 358 (2000) 2873-2911.

[2] Y. Cao, W. Tan, Z. Wu, Aircraft icing: An ongoing threat to aviation safety, Aerosp. Sci. Technol. 75 (2018) 353-385.

[3] W. Kong, H. Liu, Unified icing theory based on phase transition of supercooled water on a substrate, Int. J. Heat Mass Transfer 123 (2018) 896-910.

[4] Y. Zhao, Q. Guo, T. Lin, P. Cheng, A review of recent literature on icing phenomena: Transport mechanisms, their modulations and controls, Int. J. Heat Mass Transfer 159 (2020) 120074.

[5] Y. Cao, Z. Wu, Y. Su, Z. Xu, Aircraft flight characteristics in icing conditions, Prog. Aerosp. Sci. 74 (2015) 62-80.

[6] Y.M. Lee, J.H. Lee, L.P. Raj, J.H. Jo, R.S. Myong, Large-eddy simulations of complex aerodynamic flows over multi-element iced airfoils, Aerosp. Sci. Technol. 109 (2021) 106417.

[7] M.B. Bragg, A.P. Broeren, L.A. Blumenthal, Iced-airfoil aerodynamics, Prog. Aerosp. Sci. 41 (2005) 323-362.
[8] L. Gao, Y. Liu, H. Hu, An experimental investigation of dynamic ice accretion process on a wind turbine airfoil model considering various icing conditions, Int. J. Heat Mass Transfer 133 (2019) 930-939.
[9] Y. Liu, L. Li, W. Chen, W. Tian, H. Hu, An experimental study on the aerodynamic performance degradation of a UAS propeller model induced by ice accretion process, Exp. Therm Fluid Sci. 102 (2019) 101-112.
[10] A. Lampton, J. Valasek, Prediction of icing effects on the lateral/directional stability and control of light airplanes, Aerosp. Sci. Technol. 23 (2012) 305-311.
[11] T.P. Ratvasky, B.P. Barnhart, S. Lee, Current methods modeling and simulating icing effects on aircraft performance, stability, control, J. Aircr. 47 (2010) 201-211.
[12] B. Sengupta, L.P. Raj, M. Cho, C. Son, T. Yoon, K. Yee, R.S. Myong, Computational simulation of ice accretion and shedding trajectory of a rotorcraft in forward flight with strong rotor wakes, Aerosp. Sci. Technol. 119 (2021) 107140.
[13] G.B. Ahn, K.Y. Jung, R.S. Myong, H.B. Shin, W.G. Habashi, Numerical and experimental investigation of ice accretion on rotorcraft engine air intake, J. Aircr. 52 (2015) 903-909.
[14] L. Prince Raj, E. Esmaeilifar, H. Jeong, R.S. Myong, Computational simulation of glaze ice accretion on a rotorcraft engine intake in large supercooled droplet icing conditions, in: AIAA SCITECH 2022 Forum, 2022.
[15] B.L. Messinger, Equilibrium temperature of an unheated icing surface as a function of air speed, J. Aeronaut. Sci. 20 (1953) 29-42.
[16] S.K. Thomas, R.P. Cassoni, C.D. MacArthur, Aircraft anti-icing and de-icing techniques and modeling, J. Aircr. 33 (1996) 841-854.
[17] X. Bu, G. Lin, X. Shen, Z. Hu, D. Wen, Numerical simulation of aircraft thermal anti-icing system based on a tight-coupling method, Int. J. Heat Mass Transfer 148 (2020) 119061.
[18] M. Pourbagian, W.G. Habashi, Aero-thermal optimization of in-flight electro-thermal ice protection systems in transient de-icing mode, Int. J. Heat Fluid Flow 54 (2015) 167-182.
[19] R. Roy, L.P. Raj, J.H. Jo, M.Y. Cho, J.H. Kweon, R.S. Myong, Multiphysics anti-icing simulation of a CFRP composite wing structure embedded with thin etched-foil electrothermal heating films in glaze ice conditions, Compos. Struct. 276 (2021) 114441.
[20] L.P. Raj, K. Yee, R.S. Myong, Sensitivity of ice accretion and aerodynamic performance degradation to critical physical and modeling parameters affecting airfoil icing, Aerosp. Sci. Technol. 98 (2020) 105659.

[21] S.K. Jung, L.P. Raj, A. Rahimi, H. Jeong, R.S. Myong, Performance evaluation of electrothermal anti-icing systems for a rotorcraft engine air intake using a meta model, Aerosp. Sci. Technol. 106 (2020) 106174.
[22] J.S. Lee, H. Jo, H.S. Choe, D.S. Lee, H. Jeong, H.R. Lee, J.H. Kweon, H. Lee, R.S. Myong, Y. Nam, Electro-thermal heating element with a nickel-plated carbon fabric for the leading edge of a wing-shaped composite application, Compos. Struct. 289 (2022) 115510.
[23] T. Verstraete, S. Scholl, Stability analysis of partitioned methods for predicting conjugate heat transfer, Int. J. Heat Mass Transfer 101 (2016) 852-869.
[24] W. Wright, User's manual for LEWICE version 3.2, NASA CR-214255, NASA Glenn Research Center, 2008.
[25] T. Reid, G.S. Baruzzi, W.G. Habashi, FENSAP-ICE: unsteady conjugate heat transfer simulation of electrothermal de-icing, J. Aircr. 49 (2012) 1101-1109.
[26] L. Bennani, P. Trontin, R. Chauvin, P. Villedieu, A non-overlapping optimized Schwarz method for the heat equation with non linear boundary conditions and with applications to de-icing, Comput. Math. Appl. 80 (2020) 1500-1522.
[27] O. Harireche, P. Verdin, C.P. Thompson, D.W. Hammond, Explicit finite volume modeling of aircraft anti-icing and de-icing, J. Aircr. 45 (2008) 1924-1936.
[28] F. Morency, F. Tezok, I. Paraschivoiu, Heat and mass transfer in the case of anti-icing system simulation, J. Aircr. 37 (2000) 245-252.
[29] G. Gori, M. Zocca, M. Garabelli, A. Guardone, G. Quaranta, PoliMIce: A simulation framework for three-dimensional ice accretion, Appl. Math. Comput. 267 (2015) 96-107.
[30] R. Henry, Development of an electrothermal de-icing/anti-icing model, in: 30th Aerospace Sciences Meeting and Exhibit, 1992.
[31] J. Huang, T.G. Keith Jr, K.J. De Witt, Efficient finite element method for aircraft deicing problems, J. Aircr. 30 (1993) 695-704.
[32] R. Roelke, T. Keith Jr, K. De Witt, W. Wright, Efficient numerical simulation of a one-dimensional electrothermal deicer pad, J. Aircr. 25 (1988) 1097-1105.
[33] G.-L. Lei, W. Dong, M. Zheng, Z.-Q. Guo, Y.-Z. Liu, Numerical investigation on heat transfer and melting process of ice with different porosities, Int. J. Heat Mass Transfer 107 (2017) 934-944.
[34] W. Wright, K. Dewitt, J. KEITH, T, Numerical simulation of icing, deicing, and shedding, in: 29th Aerospace Sciences Meeting, 1991.
[35] Y. Bourgault, W.G. Habashi, J. Dompierre, G.S. Baruzzi, A finite element method study of Eulerian droplets impingement models, Int. J. Numer. Methods Fluids 29 (1999) 429-449.
[36] Y. Bourgault, H. Beaugendre, W.G. Habashi, Development of a shallow-water icing model in FENSAP-ICE, J. Aircr. 37 (2000) 640-646.

[37] T.G. Myers, Extension to the Messinger model for aircraft icing, AIAA J. 39 (2001) 211-218.
[38] T.G. Myers, J.P. Charpin, A mathematical model for atmospheric ice accretion and water flow on a cold surface, Int. J. Heat Mass Transfer 47 (2004) 5483-5500.
[39] R. Chauvin, L. Bennani, P. Trontin, P. Villedieu, An implicit time marching Galerkin method for the simulation of icing phenomena with a triple layer model, Finite Elem. Anal. Des. 150 (2018) 20-33.
[40] X. Shen, H. Wang, G. Lin, X. Bu, D. Wen, Unsteady simulation of aircraft electro-thermal deicing process with temperature-based method, Proc. Inst. Mech. Eng., Part G: J. Aerosp. Eng. 234 (2020) 388-400.
[41] S.K. Jung, R.S. Myong, A second-order positivity-preserving finite volume upwind scheme for air-mixed droplet flow in atmospheric icing, Comput. Fluids 86 (2013) 459-469.
[42] L.P. Raj, J. Lee, R.S. Myong, Ice accretion and aerodynamic effects on a multi-element airfoil under SLD icing conditions, Aerosp. Sci. Technol. 85 (2019) 320-333.
[43] Y. Liu, K. Zhang, W. Tian, H. Hu, An experimental investigation on the dynamic ice accretion and unsteady heat transfer over an airfoil surface with embedded initial ice roughness, Int. J. Heat Mass Transfer 146 (2020) 118900.
[44] Y. Liu, K. Zhang, W. Tian, H. Hu, An experimental study to characterize the effects of initial ice roughness on the wind-driven water runback over an airfoil surface, Int. J. Multiphase Flow 126 (2020) 103254.
[45] J. Shin, T.H. Bond, Experimental and computational ice shapes and resulting drag increase for a NACA 0012 airfoil, National Aeronautics and Space Administration, 1992.
[46] B. John, P. Senthilkumar, S. Sadasivan, Applied and theoretical aspects of conjugate heat transfer analysis: a review, Arch. Comput. Methods Eng. 26 (2019) 475-489.
[47] L. Cheung Yau, Conjugate Heat Transfer with the Multiphysics Coupling Library preCICE, Technical University of Munich (2016).
[48] Y. Liu, H. Hu, An experimental investigation on the unsteady heat transfer process over an ice accreting airfoil surface, Int. J. Heat Mass Transfer 122 (2018) 707-718.
[49] L. Li, Y. Liu, Z. Zhang, H. Hu, Effects of thermal conductivity of airframe substrate on the dynamic ice accretion process pertinent to UAS inflight icing phenomena, Int. J. Heat Mass Transfer 131 (2019) 1184-1195.
[50] X. Shen, Y. Zeng, G. Lin, Z. Mu, D. Wen, Effects of skin heat conduction on aircraft icing process, Proc. Inst. Mech. Eng., Part G: J. Aerosp. Eng. 235 (2021) 1306-1317.
[51] M.N. Özısık, Heat conduction, John Wiley & Sons, 1993.
[52] W. Wright, K. Al-Khalil, D. Miller, W. Wright, K. Al-Khalil, D. Miller, Validation of NASA thermal ice protection computer codes. II-LEWICE/Thermal, in 35th Aerospace Sciences Meeting and Exhibit, 2002.

[53] H. Beaugendre, F. Morency, W.G. Habashi, P. Benquet, Roughness implementation in FENSAP-ICE: Model calibration and influence on ice shapes, J. Aircr. 40 (2003) 1212-1215.
[54] N. Suzzi, G. Croce, Numerical simulation of film instability over low wettability surfaces through lubrication theory, Physics of Fluids 31 (2019) 122106.